

GFDL's CM2 Global Coupled Climate Models, Part 3: Tropical Pacific Climate and ENSO

ANDREW T. WITTENBERG*, ANTHONY ROSATI, NGAR-CHEUNG LAU, AND JEFFREY J. PLOSHAY

NOAA Geophysical Fluid Dynamics Laboratory, Princeton University, Princeton, New Jersey

Submitted to the *Journal of Climate*

ABSTRACT

Multicentury integrations from two global coupled ocean/atmosphere/land/ice models (CM2.0 and CM2.1, developed at the Geophysical Fluid Dynamics Laboratory) are described in terms of their tropical Pacific climate and El Niño/Southern Oscillation (ENSO). The integrations are run without flux adjustments and provide generally realistic simulations of tropical Pacific climate. The observed annual-mean trade winds and precipitation, sea surface temperature, surface heat fluxes, surface currents, equatorial undercurrent, and subsurface thermal structure are well captured by the models. Some biases are evident, including a cold SST bias along the equator, a warm bias along the coast of South America, and a westward extension of the trade winds relative to observations. Along the equator, the models exhibit a robust, westward-propagating annual cycle of SST and zonal winds. During boreal spring, excessive rainfall south of the equator is linked to an unrealistic reversal of the simulated meridional winds in the east, and a stronger-than-observed semiannual signal is evident in the zonal winds and equatorial undercurrent.

Both CM2.0 and CM2.1 have a robust ENSO with multidecadal fluctuations in amplitude, an irregular period between 2 and 5 years, and a distribution of SST anomalies that is skewed toward warm events as observed. The evolution of subsurface temperature and current anomalies is also quite realistic. However, the simulated ENSO events are too strong, too weakly damped by surface heat fluxes, and not as clearly phase-locked to the end of the calendar year as in observations. The simulated patterns of tropical Pacific SST, wind stress, and precipitation variability are displaced 20° – 30° west of the observed patterns, as are the simulated ENSO teleconnections to wintertime 200 hPa heights over Canada and the northeastern Pacific Ocean. Despite this, the impacts of ENSO on summertime and wintertime precipitation outside the tropical Pacific appear to be well simulated.

1 Introduction

The tropical Pacific is a key region for understanding and predicting global climate variations. With its intense precipitation and enormous size, this region directly and indirectly affects weather, ecosystems, agriculture, and human populations around the globe (Diaz and Markgraf 2000; Hsu and Moura 2001; Alexander et al. 2002; Barsugli and Sardeshmukh 2002). In particular the El Niño/Southern Oscillation (ENSO), which paleorecords suggest has existed for at least 10^5 years (Cole 2001; Tudhope et al. 2001), is the earth's dominant climate fluctuation on interannual time scales (Rothstein et al. 1998). Routine observations of the tropical Pacific (McPhaden et al. 1998), operational forecasts of ENSO and its global impacts (Latif et al. 1998; Goddard et al. 2001), and projections of future climate change (Easterling et al. 2000; IPCC 2001) all underscore the importance of ENSO for climate monitoring, climate forecasting, and climate change. Thus a key test of a comprehensive

global coupled general circulation model (CGCM) is whether it provides accurate simulations of tropical Pacific climate and ENSO.

Yet realistic CGCM simulations of the tropical Pacific have proved elusive. Strong ocean-atmosphere interactions in this region, which lend predictability to the atmosphere, also make the climate system highly sensitive to errors in the component models. Air-sea feedbacks can amplify small biases and generate sizable drifts away from the observed mean state (Dijkstra and Neelin 1995; Philander et al. 1996). These drifts, in combination with approximations in the model physics, can then affect the simulation of ENSO (Moore 1995; Fedorov and Philander 2000; Wittenberg 2002), as well as the phenomena that perturb ENSO—such as the Madden-Julian Oscillation and westerly wind bursts in the west Pacific. Climate drifts can also change how ENSO influences tropical precipitation, altering the atmospheric teleconnections that carry the ENSO signal around the globe.

As documented in recent intercomparison studies (AchutaRao et al. 2000; Latif et al. 2001; AchutaRao and Sperber 2002; Davey et al. 2000, 2002; Hannachi et al. 2003), common problems in CGCMs include (1)

*Corresponding author address: Dr. Andrew T. Wittenberg, NOAA Geophysical Fluid Dynamics Laboratory, Princeton University, P.O. Box 308, Forrestal Campus, U.S. Route 1, Princeton, NJ, 08542. E-mail: Andrew.Wittenberg@noaa.gov

a cold sea surface temperature (SST) bias in the equatorial central Pacific; (2) a warm SST bias near the coast of South America; (3) an overly-strong (“double”) Intertropical Convergence Zone (ITCZ) south of the equator in the eastern Pacific; (4) a diffuse oceanic thermocline; (5) a weak equatorial undercurrent; (6) a weak annual cycle of SST and winds in the eastern Pacific, or a semi-annual cycle instead of annual; (7) a westward shift of ENSO anomaly patterns relative to observations; (8) a weak ENSO with a period that is too short and too regular in time; and (9) ENSO SST anomalies that are not skewed strongly enough toward warm events.

Development of the latest GFDL CGCMs, CM2.0 and CM2.1, represents a significant effort toward addressing these problems—subject to the constraints of a global approach that also demands accurate simulations outside the tropical Pacific. A rather unusual aspect of this development has been the dedication of the component modelers to formulating a realistic fully-coupled system, capable of simulating climate on time scales ranging from weeks to centuries (Delworth et al. 2005; Stouffer et al. 2005). The result is a unified model framework with significant utility for seasonal-to-interannual forecasts as well as projections of future climate change.

The purpose of this paper is to evaluate the tropical Pacific climate, ENSO, and ENSO teleconnections in multicentury control integrations of these two new models, subject to 1990 radiative conditions. Results are shown from both models, due to their relevance to the community (both models are being used for the 2007 IPCC Assessment, and for operational ENSO forecasts¹), for comparison (important differences between the models lend insight into the climate of the tropical Pacific), and for continuity (the models represent a bridge between past and future climate modeling at GFDL). The ENSO forecast skill of the models and the tropical Pacific response to future radiative forcings will be covered in future papers.

2 Model description

The model formulations are described in detail in Delworth et al. (2005), so we need only comment here on a few aspects of particular relevance to the tropical Pacific.

The ocean components of CM2.0 and CM2.1 are known as OM3.0 and OM3.1 (Gnanadesikan et al. 2005; Griffies et al. 2005). Both are based on Modular Ocean Model version 4 (MOM4) code, with 50 vertical levels and a $1^\circ \times 1^\circ$ horizontal B-grid telescoping to $1/3^\circ$ meridional spacing near the equator (Fig. 1). Sub-grid scale parameterizations include KPP vertical mixing (Large

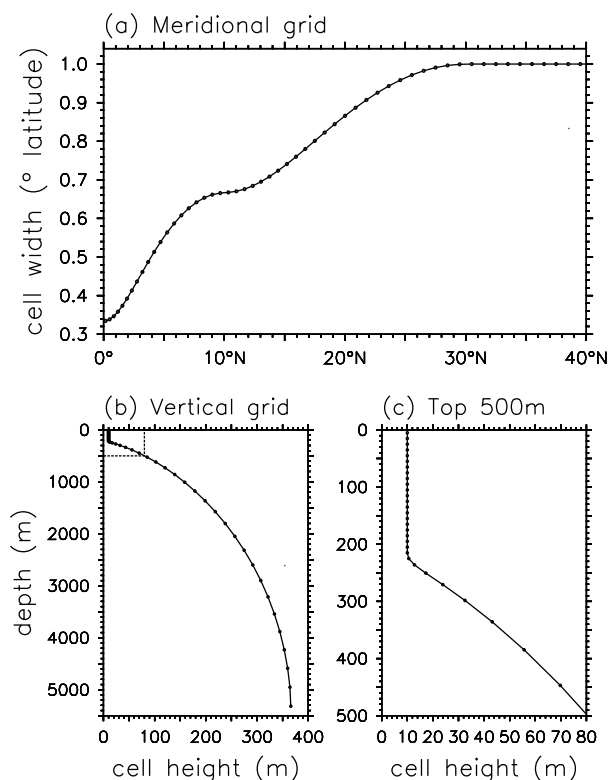


FIGURE 1: Grid cell spacings for the OM3 ocean component of the coupled models.

et al. 1994), neutral physics (Gent and McWilliams 1990; Griffies et al. 1998; Griffies 1998), and a spatially-dependent anisotropic viscosity (Large et al. 2001). Fluxes to the atmosphere are computed on the ocean model timestep, which is 1 hour in OM3.0, 2 hours in OM3.1. Insolation varies diurnally, and the short-wave penetration depth depends on a prescribed spatially-varying climatological ocean color (Morel and Antoine 1994; Sweeney et al. 2004). Both models have an explicit free surface, with true freshwater fluxes exchanged between the atmosphere and ocean. The wind stress at the ocean surface is computed using the velocity of the wind relative to the surface currents. OM3.1 has reduced values of horizontal viscosity outside the tropics, and has a constant neutral diffusivity of $600 \text{ m}^2 \text{ s}^{-1}$ which is generally larger than the non-constant values used in OM3.0.

The primary difference between the CGCMs is in the atmosphere component. CM2.0 uses the AM2p12b atmosphere model (GAMDT 2005, with modifications listed in Delworth et al. 2005), which consists of a B-grid dynamical core with 24 vertical levels, 2.5° longitude by 2° latitude grid spacing, a K-profile planetary boundary layer scheme (Lock et al. 2000), relaxed Arakawa Schubert convection (Moorthi and Suarez 1992), and a pa-

¹Hindcast evaluation metrics and real-time forecasts are available from http://www.gfdl.noaa.gov/~rgg/si_workdir/Forecasts.html.

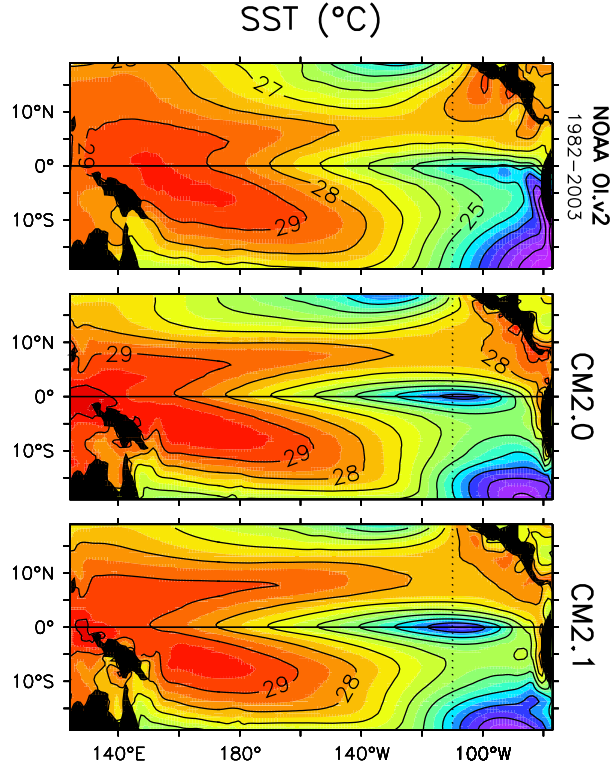


FIGURE 2: Annual mean sea surface temperatures ($^{\circ}\text{C}$) over the tropical Pacific. Observations correspond to the 1982-2003 average from the OI.v2 analysis of Reynolds et al. (2002). Dotted line corresponds to the annual cycle section of Fig. 14.

parameterization of the vertical momentum transport by cumulus convection. CM2.1 uses the AM2p13 atmosphere model, which has essentially the same spatial resolution and physical packages as AM2p12b, but substitutes a finite-volume dynamical core (Lin 2004). Other differences between the atmospheric models include a retuning of the cloud scheme and changes in the land model (Delworth et al. 2005).

The two coupled control simulations are initialized at year 1 as described in Delworth et al. (2005), and then integrated forward in time subject to 1990 values of trace gases, insolation, aerosols, and land cover. No flux adjustments are employed. In what follows, model statistics are computed using the first 300 years of each run.

3 Annual mean

a. SST and precipitation

Fig. 2 shows the annual mean SST over the tropical Pacific from the models and observations. Each model shows a well-developed equatorial cold tongue, and a warm pool in the west that extends eastward along 5°N –

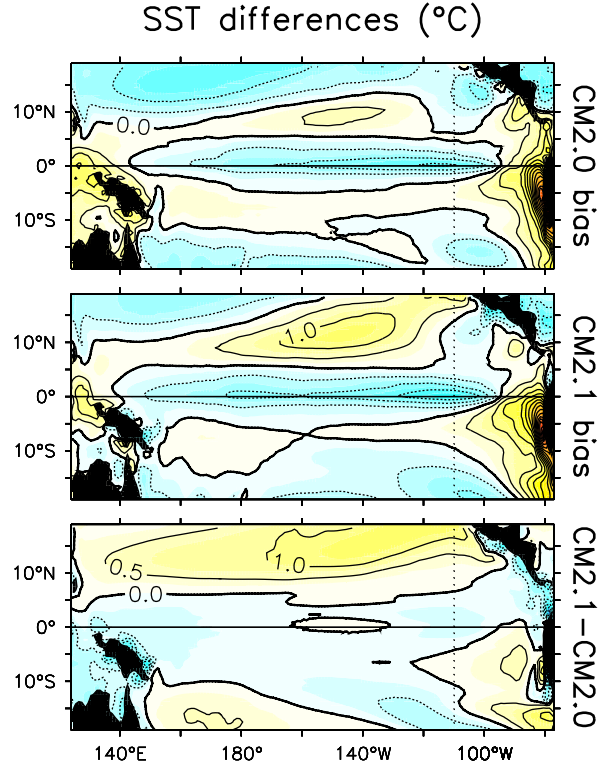


FIGURE 3: Top two rows: annual mean SST biases ($^{\circ}\text{C}$) of the coupled simulations, with respect to the OI.v2 observations in the top panel of Fig. 2. Bottom row: difference between the CM2.1 and CM2.0 SSTs. Contour interval is 0.5°C , with shading incremented every half-contour.

12°N . The west Pacific warm pools simulated by the models do not extend as far north as observed. As in many CGCMs, the simulated equatorial cold tongue is too strong and extends too far west. The equatorial cold SST bias approaches 1 – 2°C in the central/eastern Pacific, and is a bit stronger in CM2.1 than in CM2.0 (Fig. 3). In both models there is a strong warm bias near South America, approaching 7°C at the Peru coast. The SSTs are also too warm in the central Pacific near 10°N . Away from the equator, the SSTs are generally warmer in CM2.1 than CM2.0 (see also Delworth et al. 2005).

Fig. 4 shows the annual mean rainfall over the tropical Pacific. The models show strong precipitation in the far western Pacific and along the South Pacific Convergence Zone (SPCZ) and northern ITCZ regions. These features are generally stronger than observed, as is the “double ITCZ” in the east along 5°S . There is too much rainfall near New Guinea and South America, and too little rainfall along the equator in the central Pacific. The precipitation biases are largely coincident with local SST biases: there is too little precipitation on the equator where SSTs are too cold, and too much precipitation in the far west,

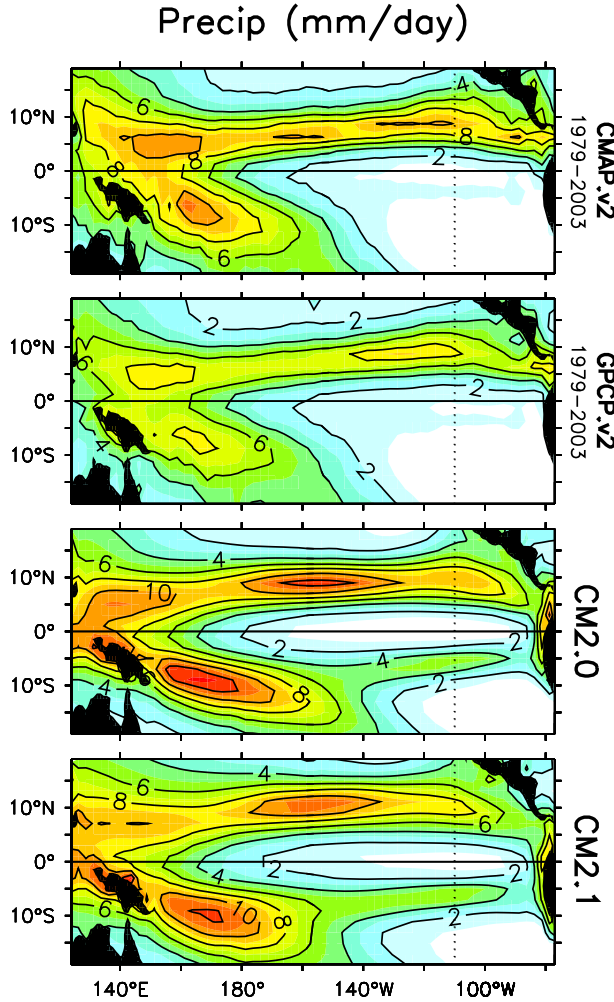


FIGURE 4: Annual mean precipitation (mm day^{-1}) over the tropical Pacific. Observations correspond to time averages from the CMAP.v2 analysis (Xie and Arkin 1996, 1997) and the GPCP.v2 analysis (Huffman et al. 1997).

far east, and off-equator where SSTs are too warm. Compared to CM2.0, CM2.1 shows less rainfall in the ITCZ, SPCZ, and western Pacific, and more rainfall along the equator, all of which are in better agreement with the observations; but CM2.1 also shows a slightly stronger double ITCZ bias in the southeast.

b. Surface wind stress

Fig. 5 shows the zonal component of the annual mean surface wind stress (τ_x). The mean equatorial τ_x is well simulated when compared with the ERA40 observations, with peak easterlies of about 0.5–0.6 dPa occurring near 150°W, and weak westerlies near the eastern and western boundaries. Note that the true mean wind stresses over

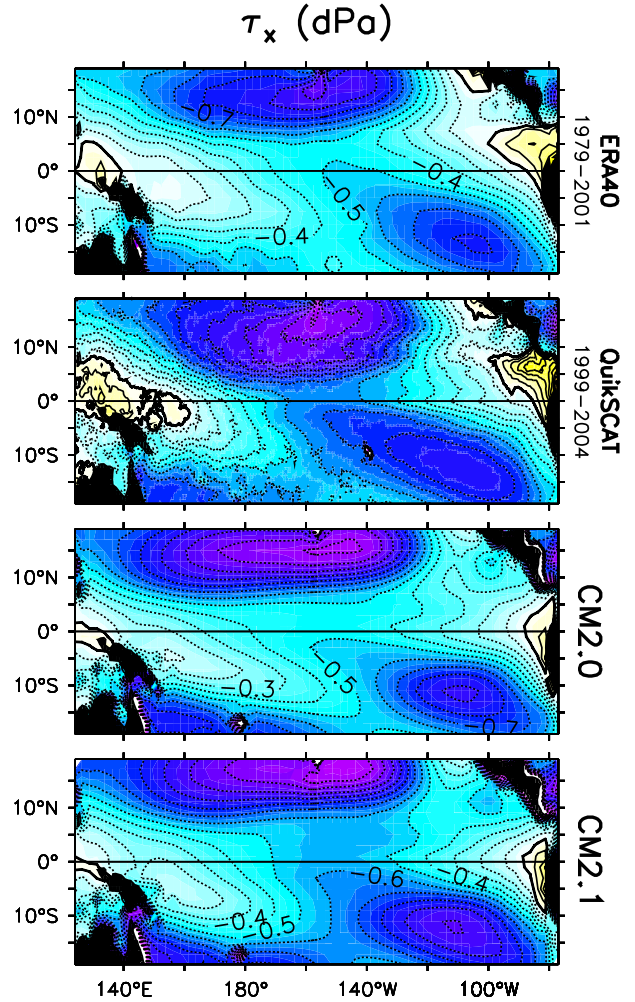


FIGURE 5: Zonal component of the annual mean surface wind stress (dPa). Observations correspond to the ECMWF 40-year reanalysis (ERA40, Simmons and Gibson 2000) averaged 1979–2001, and the SeaWinds/QuikSCAT level 3.0 product (IFREMER/CERSAT 2002) averaged Dec 1999 through Nov 2004.

the tropical Pacific are quite uncertain (Wittenberg 2004), with other observational products such as FSU (Stricherz et al. 1997; Bourassa et al. 2001) and SSM/I (Atlas et al. 1996) giving somewhat stronger zonal stresses over this period. The QuikSCAT observations (Fig. 5, second panel) also show stronger wind stresses throughout the central tropical Pacific, compared to ERA40.

Fig. 6 shows that CM2.1 generally has stronger central Pacific easterlies than CM2.0, except along 10°N due to the poleward shift of the northern core of the easterlies in CM2.1 relative to CM2.0. In both models the equatorial easterlies are zonally broader than in the observations, with the western flank of the trades extending too far west. The off-equatorial easterlies also extend too far

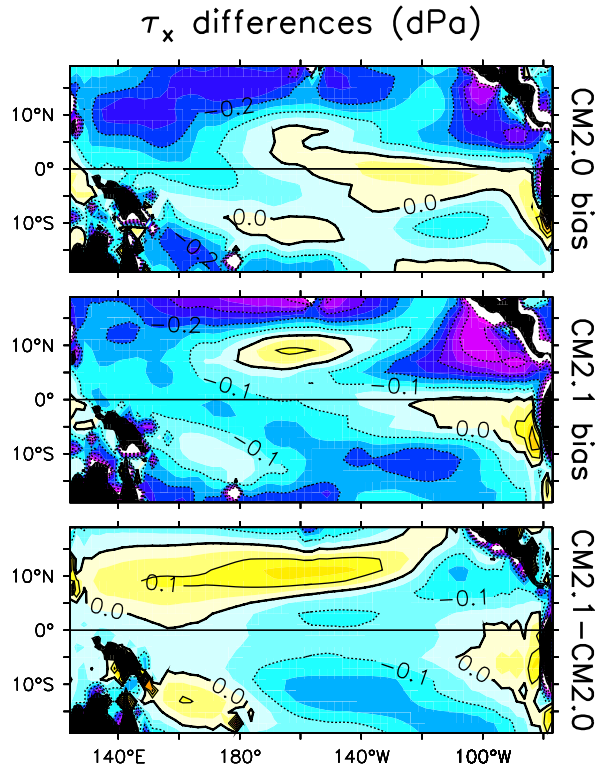


FIGURE 6: Top two rows: annual mean zonal wind stress biases (dPa) of the coupled simulations, with respect to the ERA40 observations in the top panel of Fig. 5. Bottom row: zonal wind stress difference between CM2.1 and CM2.0.

west and are too strong, giving rise to similar biases in the off-equatorial cyclonic wind stress curl. Note that the τ_x differences between CM2.0 and CM2.1 are generally larger in the extratropics than in the tropics (Delworth et al. 2005).

c. Surface heat fluxes

The annual-mean equatorial surface heat fluxes from the models and observations are shown in Fig. 7. The simulated fluxes are in reasonable agreement with the broad range of observational estimates. Consistent with the overly dry conditions on the equator in the models (Fig. 4), there is roughly $10\text{--}30\text{ W m}^{-2}$ too much solar heating in the central and eastern Pacific, and $5\text{--}10\text{ W m}^{-2}$ too much longwave cooling. In the western/central Pacific, where the simulated trade winds are too strong (Fig. 6), there is $10\text{--}30\text{ W m}^{-2}$ more evaporative cooling than observed. Conversely, in the east Pacific where the southeasterly trades are too weak (Fig. 14c), there is less evaporative cooling than in most of the observational estimates.

In the west Pacific there seems to be too little net down-

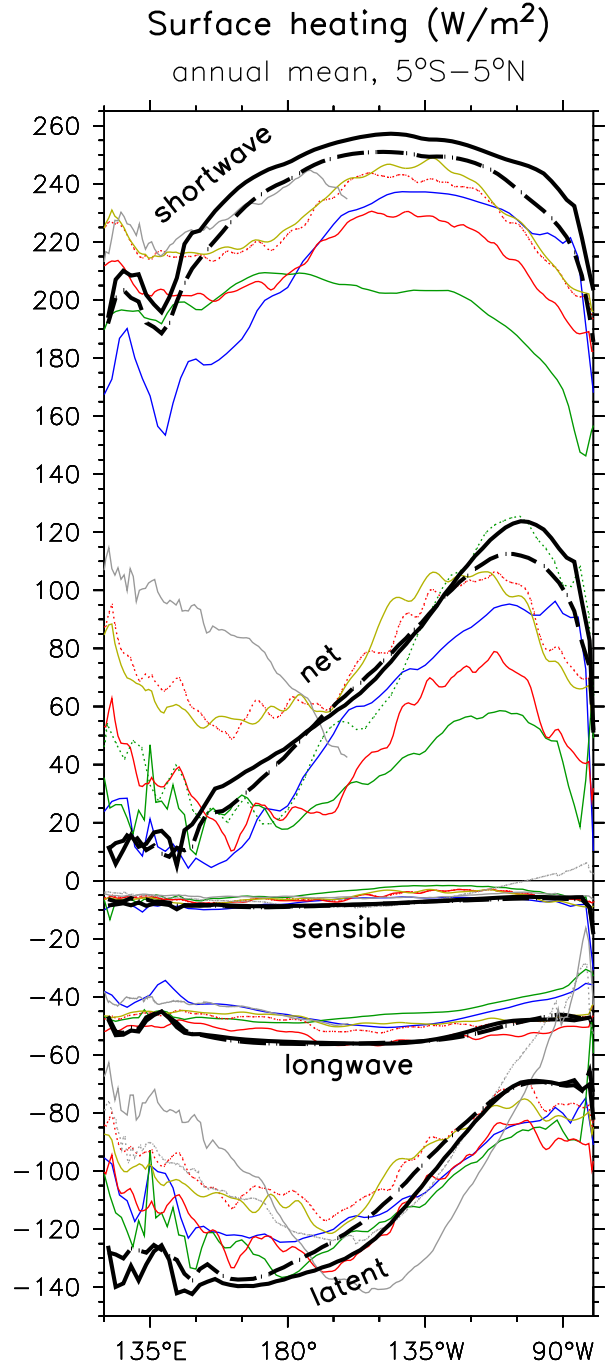


FIGURE 7: Annual mean surface heat fluxes over the Pacific, averaged $5^\circ\text{S}\text{--}5^\circ\text{N}$. Thick lines are simulations from CM2.0 (dashed) and CM2.1 (solid). Thin lines are observational estimates from the ERA40 reanalysis (1979–2001) in blue; NCEP-DOE AMIP-II reanalysis (1979–2001) in solid green; the ERBE/NCEP net surface flux (March 1985–Feb 1989 from Trenberth et al. 2001, version dated March 2003) in dotted green; Southampton Oceanography Centre (SOC) fluxes (years 1980–1997 from Josey et al. 1998) in dotted red; adjusted SOC fluxes (Solution 3 from Grist and Josey 2003) in solid red; UWM/COADS (years 1979–1993 from da Silva et al. 1994) in yellow; J-OFURO (all available years from 1990–2001, Kubota et al. 2002) in solid gray; and HOAPS-II (years 1987–2002, Grassl et al. 2000) in dotted gray.

ward heat flux in the models, despite the SST cold bias—suggesting that the excessive evaporation may be partly to blame for the cold bias in the west. Weak evaporation and excessive insolation may also contribute to the overly warm SSTs near the South American coast. However, in the central equatorial Pacific the excessive insolation *mitigates* the overly strong cold tongue in the models. This implies that the cold bias in the central equatorial Pacific must be driven by ocean dynamical cooling rather than by errors in the air-sea heat fluxes.

At the equator CM2.1 shows increased insolation—despite slightly more precipitation—than in CM2.0. CM2.1 also shows stronger evaporation (due to stronger easterlies) over the central Pacific. Although the solar and evaporative heat flux differences between the models nearly cancel over the central basin, the increased shortwave in CM2.1 does produce more net heating in the western and eastern equatorial Pacific, where CM2.1 is cooler than CM2.0. The net heat flux difference thus mainly acts to oppose the SST differences between the models.

The errors in annual-mean precipitation, surface wind stress, and surface heat fluxes are much reduced when the atmospheric model is forced by observed SSTs (GAMDT 2005, Delworth et al. 2005). Thus it appears that the biases in the coupled models are the result of a climate drift, associated with strong air-sea feedbacks over the Pacific.

d. Ocean currents

The annual-mean surface zonal currents from the models and observations are shown in Fig. 8. In the western central Pacific the models capture the general structure of the observed surface currents, including the westward South Equatorial Current (SEC) and North Equatorial Current (NEC), and the eastward North Equatorial Countercurrent (NECC). The simulated currents, however, are displaced 20–30° west of the observed currents, the simulated SEC is too weak and meridionally too wide, and in the eastern Pacific the sign of the simulated mean NECC is reversed compared to observations. In general the annual-mean surface currents are weaker in CM2.1 than in CM2.0, despite the stronger annual-mean zonal wind stress in CM2.1.

Fig. 9 shows the subsurface structure of the mean zonal currents at the equator. Compared to observations, both models show a good simulation of the annual mean equatorial undercurrent (EUC), especially at 140°W where the observed and simulated currents reach a peak value of slightly over 1 m s⁻¹. At 110°W the simulated EUC is slightly too weak, while farther west it is too strong and vertically too broad. At 165°E there is excessive vertical shear of the zonal currents over the top 100 m, associ-

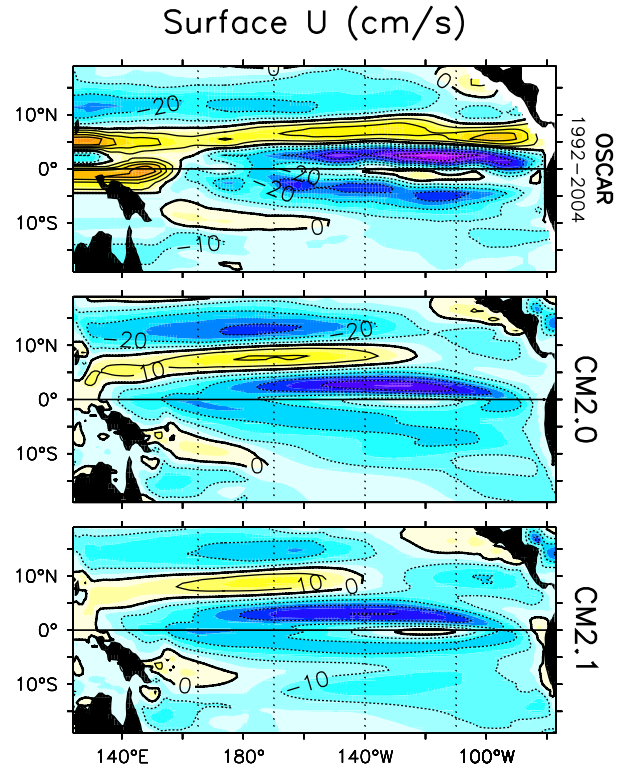


FIGURE 8: Annual-mean surface zonal currents (cm s^{-1}) for the tropical Pacific. Observations correspond to the OSCAR analysis of Bonjean and Lagerloef (2002), averaged Nov 1992 through Oct 2004. Dotted lines correspond to the longitudes in Fig. 9.

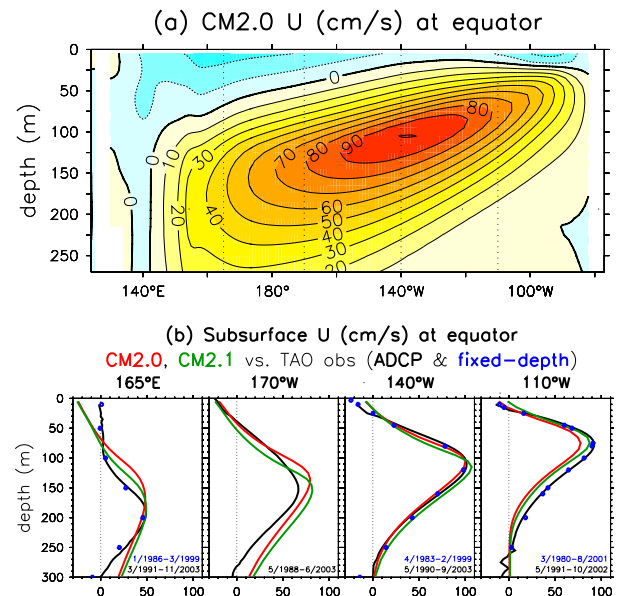


FIGURE 9: Annual-mean zonal currents (cm s^{-1}) at the equator: (a) mean values for CM2.0; (b) mean values at the four longitudes marked in (a), from CM2.0 (red), CM2.1 (green), TAO Acoustic Doppler Current Profilers (black) and TAO fixed-depth current meters (blue dots).

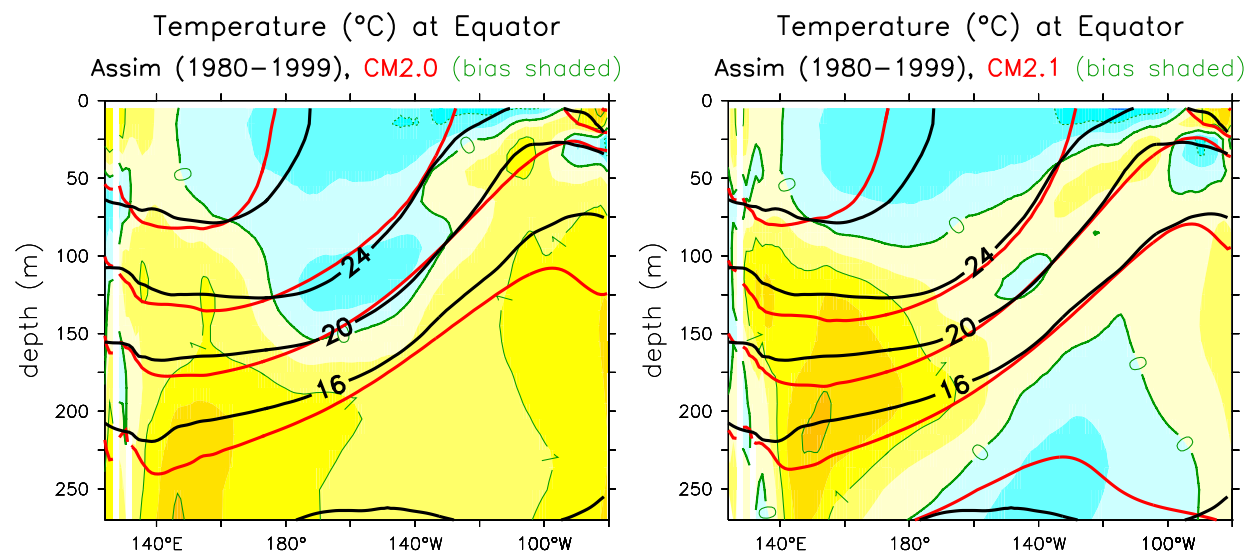


FIGURE 10: Annual-mean Pacific Ocean temperatures (°C) along the equator. Black contours indicate “observed” values from the GFDL/ARCs ocean analysis; red contours the model solution; and green contours/shading the mean temperature bias of the model relative to GFDL/ARCs.

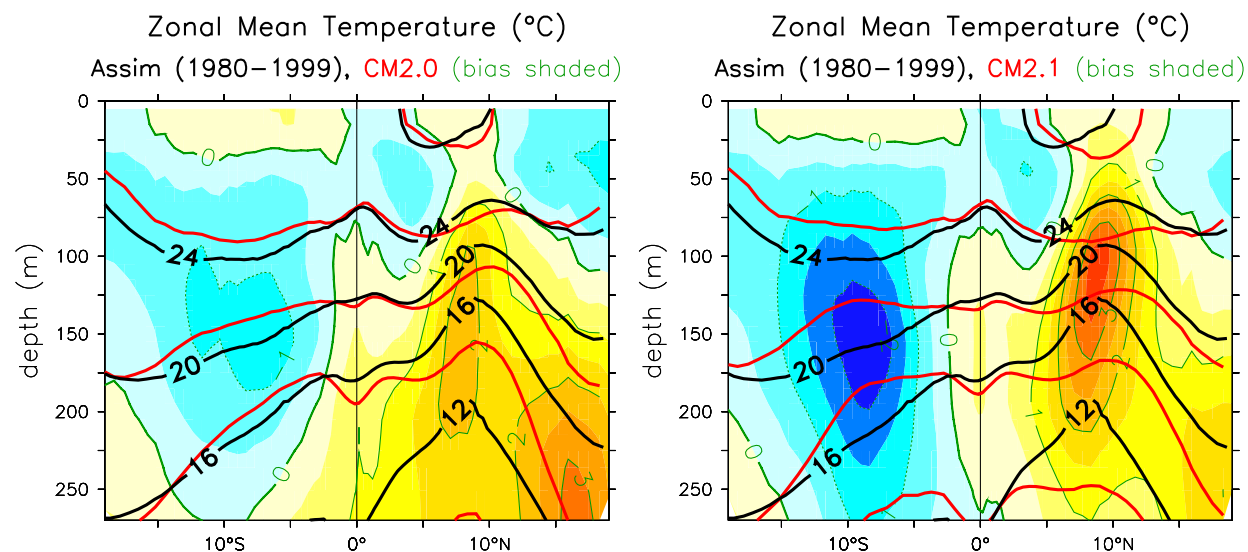


FIGURE 11: As in Fig. 10, except for ocean temperatures averaged zonally across the Pacific basin.

ated with a SEC that extends too far west in the models. CM2.1 and CM2.0 produce very similar simulations of the EUC, with CM2.1 slightly stronger in the east due to the stronger annual mean τ_x in that model (Figs. 5 and 6).

e. Subsurface temperatures

Fig. 10 shows the simulated Pacific upper-ocean temperatures along the equator, compared to the GFDL/ARC's ocean analysis². A surface cold bias is evident in the central Pacific, along with a warm bias below the thermocline. The zonal-mean depth of the 20°C isotherm is nearly correct, but the zonal slope of the thermocline is slightly too strong, consistent with the overly broad zonal extent of the simulated equatorial easterlies. The thermocline is also too diffuse in the vertical. The warm pool in the west does not extend far enough out into the basin, due to the overly strong equatorial upwelling, westward cold advection, and evaporation driven by the strong simulated easterlies. These problems are less pronounced in CM2.0, which has weaker trade winds than CM2.1. Near South America there is strong stratification in the models compared to the ocean analysis, with a surface warm bias sitting directly above a cold bias at 30 m. This problem is also reduced in CM2.0 compared to CM2.1. CM2.1, on the other hand, shows less of a cold bias in the central basin at 100 m than does CM2.0.

Fig. 11 shows the upper ocean temperatures averaged zonally across the Pacific basin. Above 75 m, both models exhibit a zonal-mean cold bias except in the vicinity of the ITCZ (8°N–10°N) and near the surface south of the equator. Between 75 m and 250 m, the models show a cold bias in the south and a warm bias in the north, associated with a meridional flattening of the isotherms compared to the ocean analysis. The strongest biases lie near the ITCZ, where the isotherms in the models do not bow upward as strongly as in the analysis, consistent with the weak NECC in the models (Fig. 8). The zonal-mean warm bias at this location approaches 4°C in CM2.1, compared to 2.5°C for CM2.0. Below 200 m, CM2.1 shows cooler zonal-mean temperatures than CM2.0.

The simulated ocean subsurface temperatures show greater differences when compared with the NCEP Pacific Ocean analysis of Behringer et al. (1998), which has a somewhat tighter annual-mean thermocline at the equator. The analogue of Fig. 10 shows increased cold/warm biases above/below the thermocline, a larger difference in the zonal thermocline slope, and stronger stratification biases above 50 m near the South American coast. Away from the equator, however, the coupled model dif-

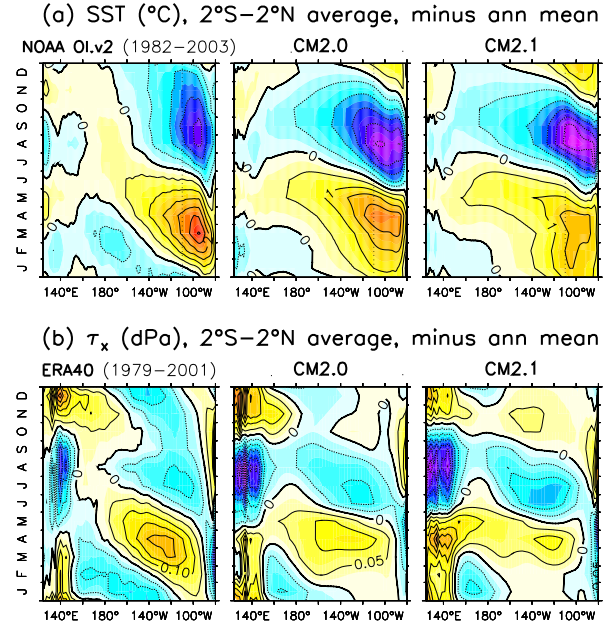


FIGURE 12: Annual cycle, averaged 2°S–2°N, of (a) SST (°C) and (b) zonal wind stress (dPa). Annual-mean values are subtracted. Observations correspond to OI.v2 (Reynolds et al. 2002) for SST, and ERA40 for wind stress.

ferences with the NCEP ocean analysis look very similar to Fig. 11.

4 Seasonal cycle

a. Equator

The annual cycle of equatorial Pacific SST is shown in Fig. 12a. In qualitative agreement with observations, both models show a robust westward-propagating annual cycle of SST in the eastern and central Pacific, and a semiannual cycle in the west. The zonal-mean annual cycle of SST is somewhat too strong in the models (see also Fig. 20), since between April and November the annual cycle of SST propagates too far west—with 0.5°C anomalies extending west the dateline instead of staying east of 160°W as observed. On the other hand, the observed 0.5°C cold anomalies near the dateline in March are not seen in the models. In the east the warm season peak is too weak compared to the cold season peak, especially in CM2.1. Apart from the warm peak in boreal spring, the phase of the seasonal cycle in the east is also shifted 1–2 months earlier in the models than in observations.

Fig. 12b shows the annual cycle of τ_x near the equator. The models capture some of the observed relaxation of the trade winds during boreal spring, though it is underestimated and exhibits less of the westward propagation

²Observed SSTs and temperature profiles assimilated into MOM4, using the three-dimensional variational scheme of Derber and Rosati (1989). Available from <http://nomads.gfdl.noaa.gov>.

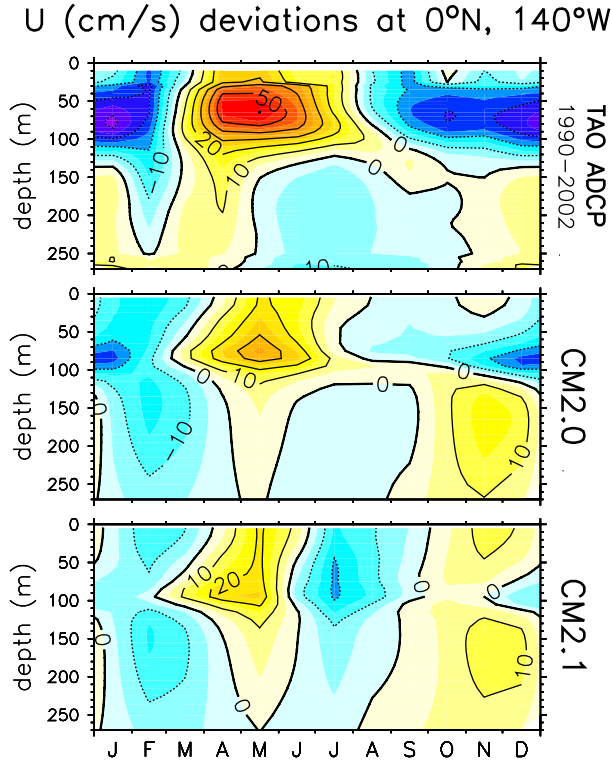


FIGURE 13: Annual cycle of zonal currents (cm s^{-1}) on the equator at 140°W . Annual mean is subtracted. Observations correspond to the 1990–2002 climatology from the TAO ADCP moored at 140°W .

seen in the observations. In the east Pacific, the strengthening of the trades during boreal summer is reasonably well captured, although the models show a westward shift of the seasonal cycle relative to the observations. CM2.1 shows stronger peak easterly deviations than observed in boreal summer. The models display more of a semiannual cycle than observed, with weaker-than-observed trades in boreal autumn and winter. In contrast, the simulated annual cycle of τ_x in the far western Pacific is stronger than observed.

The seasonal cycle of τ_x is tightly linked with that of the equatorial undercurrent. Although the models do well with the annual-mean strength of the EUC (Fig. 9), they underestimate the strength of its annual cycle (Fig. 13). That the May peak of the EUC is too weak, especially in CM2.1, is likely tied to the lack of a sudden weakening of the equatorial trade winds early in the year (Fig. 12b). Above 100 m both models show more of a semiannual cycle than observed, consistent with the excessive semiannual signal in the simulated winds.

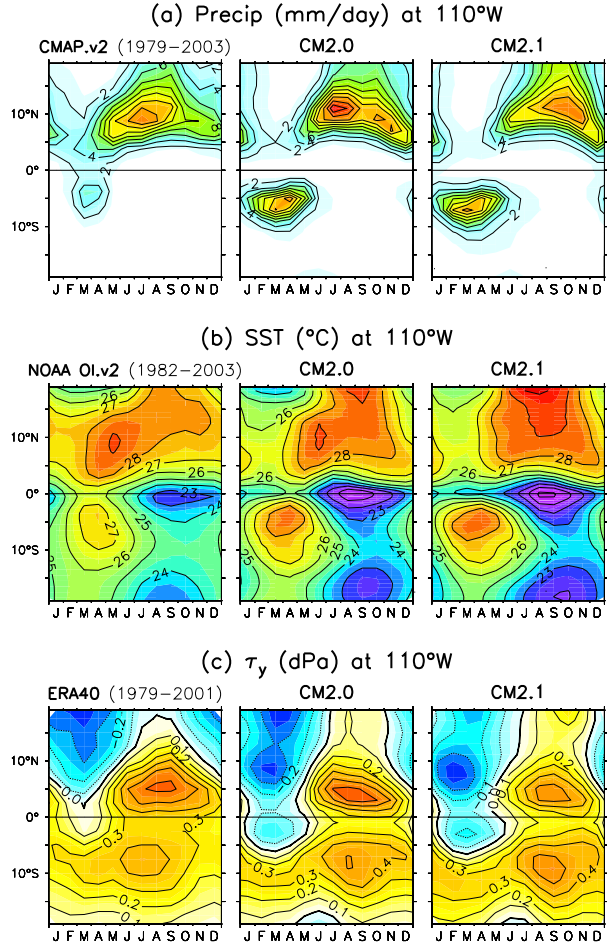


FIGURE 14: Annual cycle along 110°W of (a) rainfall (mm day^{-1}), (b) SST ($^\circ\text{C}$), and (c) meridional wind stress (dPa).

b. East Pacific

The annual cycle of precipitation in the eastern tropical Pacific is shown in Fig. 14a. The observations show a maximum north-south asymmetry of SST and rainfall during boreal summer and autumn, when the ITCZ is strongest. In March–April, the precipitation is weaker and more symmetric about the equator, with substantial precipitation observed even at the equator. While CM2.0 and CM2.1 capture most of these features, there are some obvious problems. In the southern hemisphere, both CM2.0 and CM2.1 rain too much and too far south in boreal spring, at the expense of spring precipitation at the equator and in the ITCZ. CM2.0 captures the observed July peak in ITCZ rainfall but overestimates its magnitude, while CM2.1 has roughly the right magnitude but shows the peak occurring three months too late.

Many of the errors in the simulated annual cycle of precipitation in the east Pacific are coupled to errors in the

annual cycle of SST (Fig. 14b). The observed SSTs show a strengthening of the cold tongue in boreal autumn, and a weakening in boreal spring; in March the observed climatological SSTs approach 26.5°C at the equator, but the warmest SSTs remain north of the equator. In the models the climatological equatorial SSTs stay below 25.5°C all year, and in March the warmest SSTs are south of the equator. The models also show too much of a cold tongue/ITCZ SST contrast in boreal autumn, when the ITCZ region is 1°C too warm and the cold tongue is 2°C too cold.

The seasonal biases in SST and precipitation are likewise tied to the atmospheric meridional circulation in the eastern Pacific (Fig. 14c). At the equator, the observed climatological τ_y weakens significantly in boreal spring but remains southerly all year. In contrast, the models exhibit a reversal of the equatorial τ_y in boreal spring, in tandem with the reversal of the simulated meridional gradient of SST. The minimum of τ_y at 2°S is more pronounced in the models than in observations, as is the local maximum of τ_y at 10°S, producing an overly strong wind convergence along 4–8°S which is linked to excessive precipitation during boreal spring (Fig. 14a). Compared to CM2.0, CM2.1 shows a stronger March reversal of the meridional winds, and a stronger convergence of τ_y along 4–8°S.

5 ENSO

a. Spatial patterns

The spatial patterns of tropical Pacific interannual SST variability are shown in Fig. 15. In the observations, the interannual SSTAs are strongest in the eastern equatorial Pacific and along the coast of South America. The models shift this variability westward, and both models (especially CM2.1) overestimate the interannual variability of SST throughout the tropical Pacific.

Fig. 16 shows the tropical Pacific precipitation regressed onto NINO3 SSTAs. The observations indicate wet conditions along the equator in the central and eastern Pacific during warm events, with peak rainfall anomalies just east of the dateline. Meanwhile, drier-than-normal conditions prevail away from the equator and west of 155°E. In the eastern Pacific, the observed rainfall response is meridionally asymmetric, with wet conditions north of the equator but little change in the south. While the models do show increased rainfall over the central equatorial Pacific during warm events, there are clear differences with the observations. The precipitation response is too far west—consistent with the equatorial cold bias and the westward displacement of the annual-mean convection in the models (Figs. 2–4). In the east

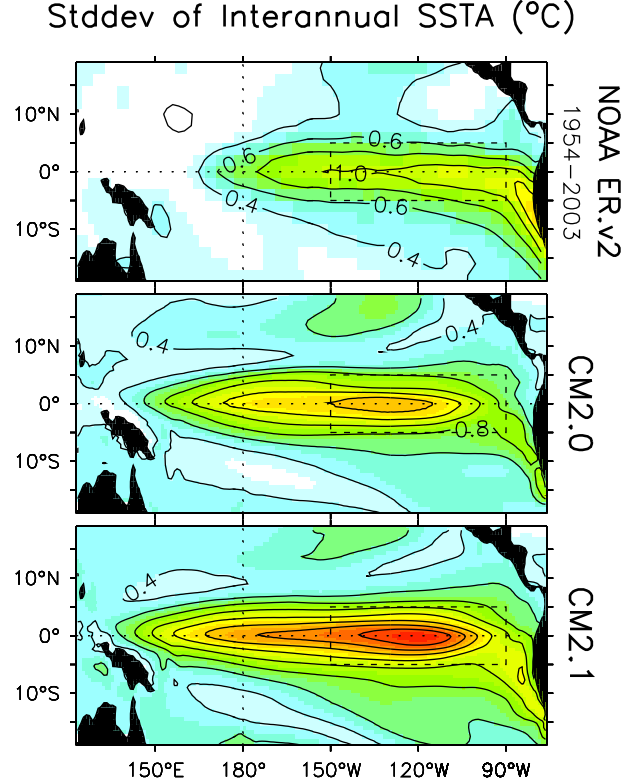


FIGURE 15: Standard deviation of interannual SST anomalies (°C). The anomalies are filtered via two applications of a 4-month running mean, transmitting 25% and 75% of the spectral amplitude at periods of 6.6 and 14 months, respectively. Observations correspond to the ER.v2 reconstruction of Smith and Reynolds (2003). The dashed box in each panel indicates the NINO3 region (150°W–90°W, 5°S–5°N).

Pacific, the rainfall anomalies are too symmetric about the equator, probably due to the south-equatorial climatological warm bias and double ITCZ. There are also clear differences between the models themselves: in the west the peak rainfall anomalies are stronger in CM2.0 than in CM2.1, while in the east the equatorial rainfall is stronger in CM2.1.

The zonal wind stress anomaly (τ'_x) response to NINO3 SSTAs is shown in Fig. 17. The observations show westerly anomalies in the equatorial central Pacific during warm events, with the peak anomalies slightly east of the dateline. The simulated equatorial westerly anomalies are too weak and too far west, and in both models the easterly anomalies south of the equator and in the east Pacific are too strong. The τ'_x response along the equator extends farther east in CM2.1 than in CM2.0, consistent with the simulated climatological and anomalous precipitation differences between the two models (Figs. 4 and 16).

Figs. 18 and 19 show the net surface heat fluxes regressed onto NINO3 SSTAs. As noted by Barnett et al.

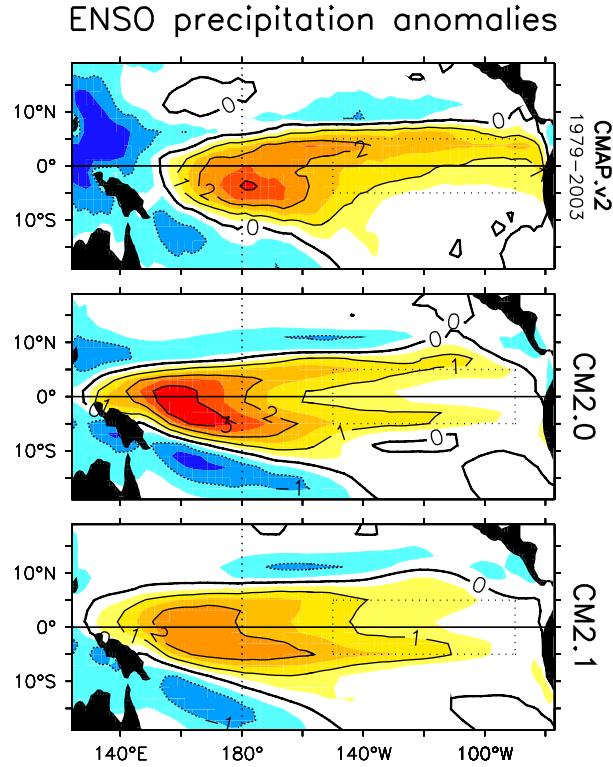


FIGURE 16: Precipitation anomalies regressed onto NINO3-averaged SST anomalies, all months included. Units are $\text{mm day}^{-1} \text{ } ^\circ\text{C}^{-1}$. Observations correspond to the CMAP.v2 precipitation anomalies regressed onto the ER.v2 SSTAs for 1979–2003.

(1991) and others, during a warm event the observed heat fluxes act to damp the zonal SSTA gradient (and thus the τ_x anomalies as well), due to increased cloudiness and evaporation in the east Pacific and reduced cloudiness in the west. This damping effect is underestimated by the models, largely because the simulated convective response is too far west (Fig. 16). During warm events, the models show increased cloud shading in the far western Pacific instead of in the central Pacific as observed; and in the far eastern equatorial Pacific, the models actually have slightly increased insolation during warm events, instead of reduced insolation as observed. Neither model has sufficient heat flux damping in the far western Pacific, where the SSTs are presumably most directly influenced by the surface heat fluxes due to the absence of strong equatorial upwelling, and where the atmosphere is presumably most sensitive to SSTAs due to the presence of warm mean SSTs and convergent surface winds. Note that CM2.1 has a somewhat weaker zonally-integrated surface heat flux damping than does CM2.0.

As was the case for the annual-mean fields in Section 3, the errors in the coupled model regression pat-

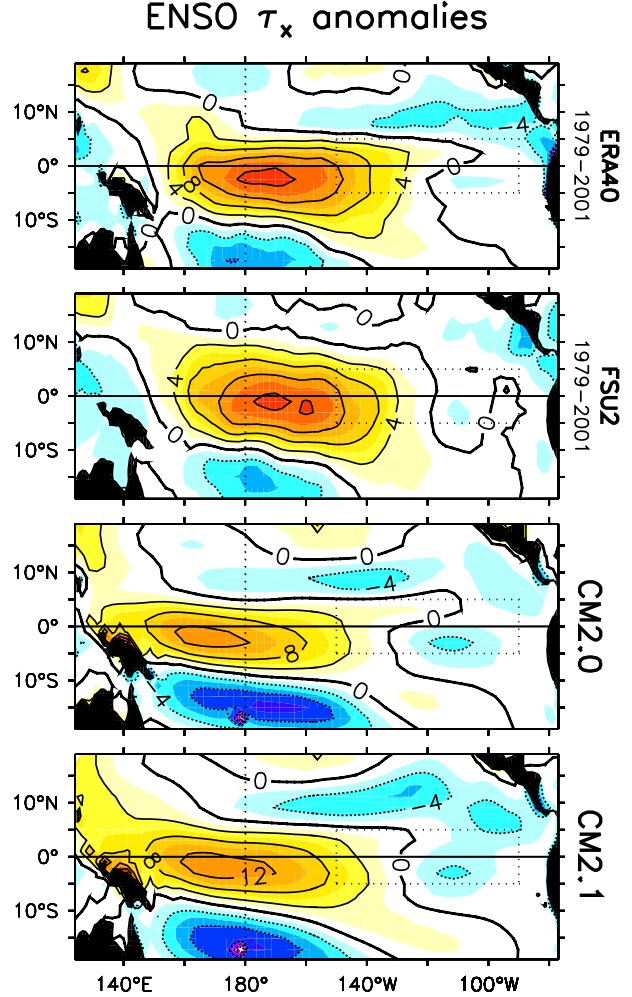


FIGURE 17: Zonal wind stress anomalies regressed onto NINO3-averaged SST anomalies, all months included. Units are $\text{mPa } ^\circ\text{C}^{-1}$. Observations are regressed onto the ER.v2 SSTAs for 1979–2001, and correspond to stress anomalies from the ERA40 reanalysis, and from the FSU2 objective analysis (Bourassa et al. 2001; Smith et al. 2004). The FSU2 stress is the FSU2 pseudostress multiplied by an air density $\rho_a = 1.2 \text{ kg m}^{-3}$ and a drag coefficient $c_d = 1.3 \times 10^{-3}$.

terns appear to arise mostly from errors in the simulated climatological SSTs—especially the equatorial cold bias which inhibits the eastward shift of convection during warm events. When the atmospheric GCMs are driven by observed SSTs, the precipitation, wind stress, and heat flux anomaly patterns agree much better with observations (GAMDT 2005; Sun et al. 2005). Yet even in this SST-driven context the atmosphere models exhibit hints of the CGCM biases—including a faint “double ITCZ” in the east along 5°S , too much shortwave radiation absorbed by the ocean along the coast of South America, and ENSO precipitation anomalies that are shifted slightly too far west along the equator.

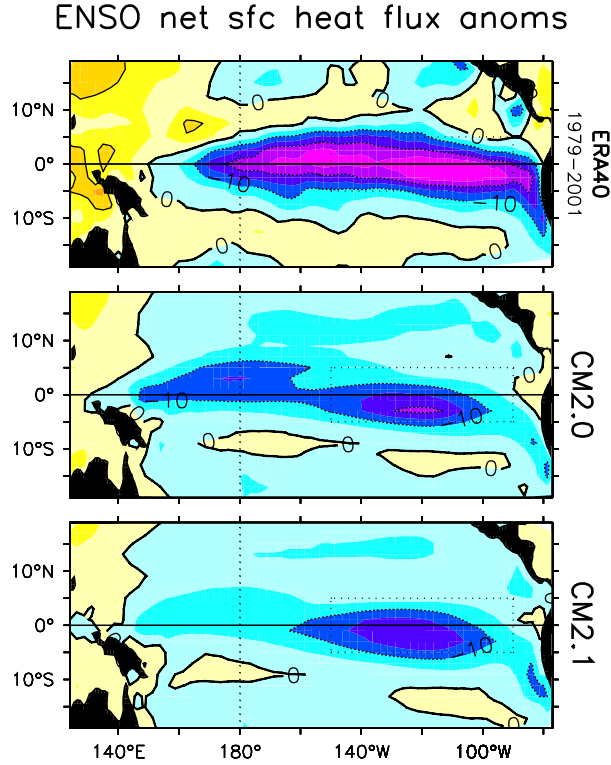


FIGURE 18: Anomalous net surface heat flux into the ocean, regressed onto NINO3-averaged SST anomalies, all months included. Units are $\text{W m}^{-2} \text{ } ^\circ\text{C}^{-1}$. Observations correspond to the ERA40 fluxes regressed onto ER.v2 SSTAs for 1979–2001.

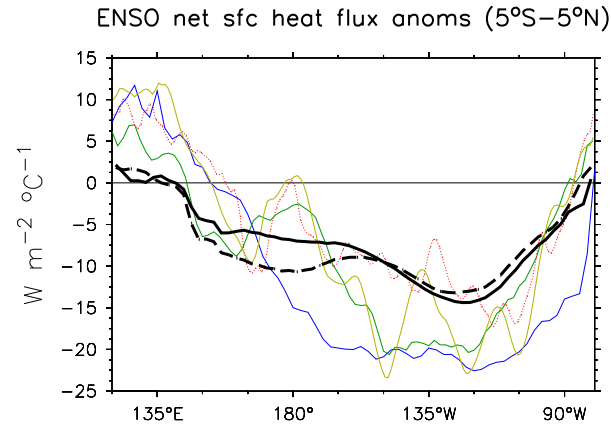


FIGURE 19: Anomalous net surface heat flux into the ocean, averaged 5°S – 5°N , regressed onto NINO3-averaged SST anomalies. All months are included in the regression. Units are $\text{W m}^{-2} \text{ } ^\circ\text{C}^{-1}$. Thick lines are the model solutions from CM2.0 (dashed) and CM2.1 (solid). Thin lines are observational estimates (regressed onto ER.v2 SSTAs) from the ERA40 (1979–2001) in blue; NCEP-DOE AMIP-II reanalysis (1979–2001) in green; SOC fluxes (years 1980–1997 from Josey et al. 1998) in dotted red; and UWM/COADS (years 1979–1993 from da Silva et al. 1994) in yellow.

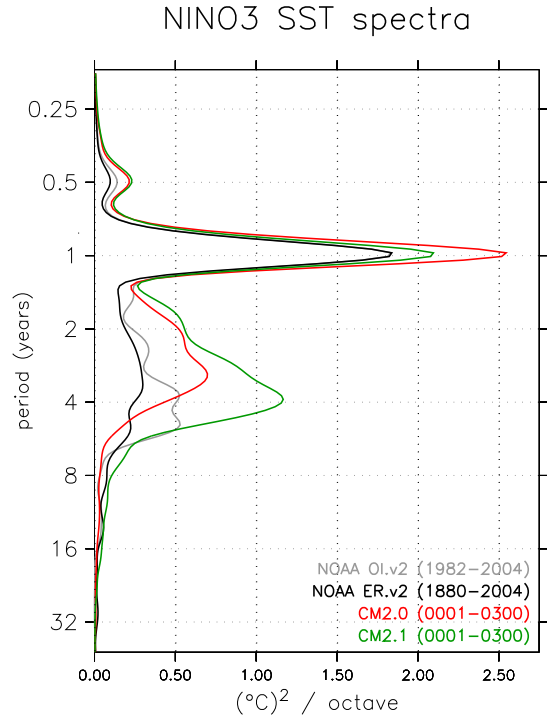


FIGURE 20: Time-mean spectra ($^\circ\text{C}^2 \text{ octave}^{-1}$) for unfiltered NINO3-average SSTs from the observations, CM2.0, and CM2.1. The spectra are based on the wavelet analyses of Figs. 21 and 22. Observations correspond to OI.v2 (1982–2004, Reynolds et al. 2002) and ER.v2 (1880–2004, Smith and Reynolds 2003).

b. Spectra

Fig. 20 shows NINO3 SST spectra for the models and observations. The observations display spectral peaks at annual and semiannual periods, as well as a broad peak in the interannual band between 2–5 years. Although the models capture these features qualitatively, there are clear differences. The amplitude of the annual cycle is nearly correct in CM2.1, despite the bias toward the cold season evident in Fig. 12a. However, the annual cycle is too strong in CM2.0, and both models show stronger semiannual variability than in observations. Both models (especially CM2.1) have overactive ENSOs compared to long-term (1880–2004) observations, but agree more favorably with the amplitude observed over the last two decades³. The peak ENSO period in CM2.1 (3.9 yr) is a good match to the recent observations, while that in CM2.0 (3.1 yr) is slightly too short.

The time evolutions of the simulated NINO3 SST spec-

³The latter period (1982–2004) is perhaps the more appropriate one to compare with the models, since the models are subjected to 1990 radiative forcings.

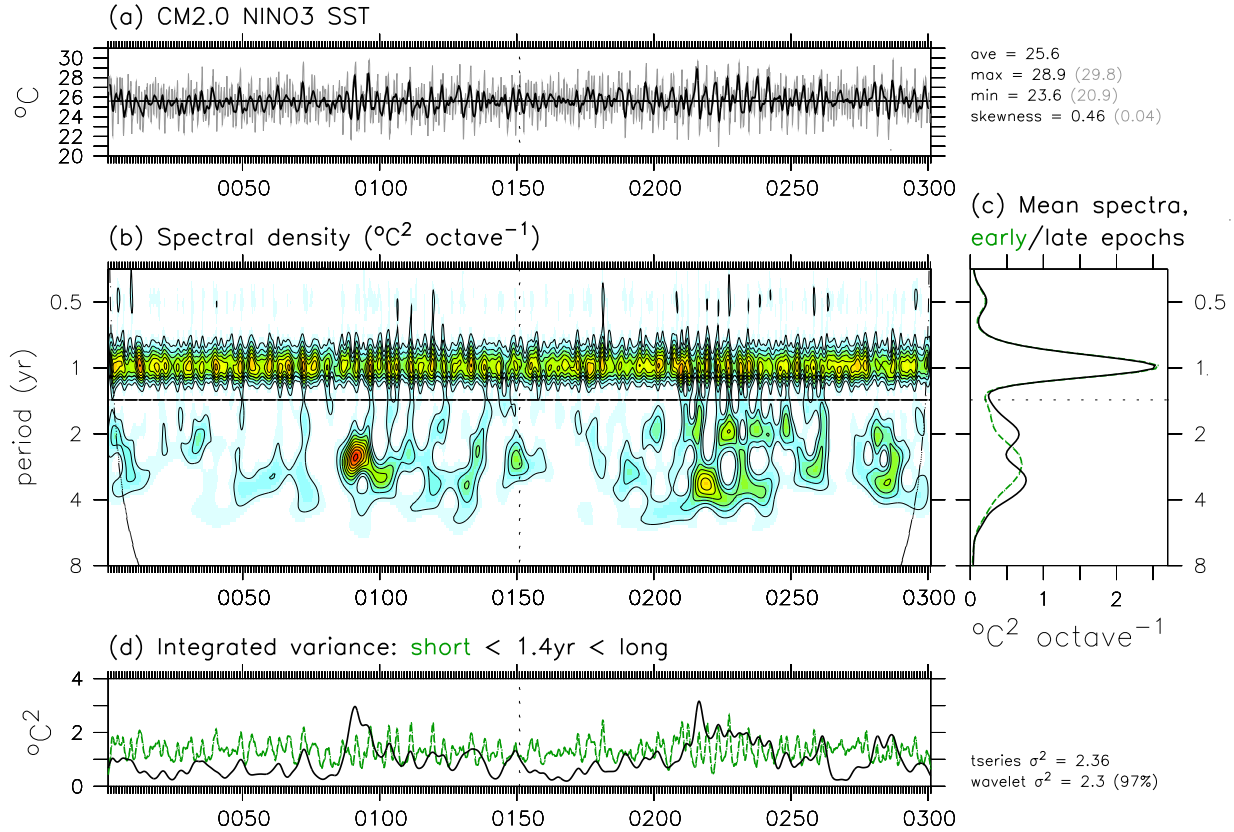


FIGURE 21: (a) Timeseries of NINO3-averaged SST as simulated by CM2.0. Gray line indicates monthly values, black line is the running annual mean. The mean, maximum, minimum, and skewness of each timeseries are listed to the right of this panel. (b) Spectral power density of the timeseries, obtained by convolution with a Morlet wavenumber-6 wavelet. The base contour line and contour interval are $0.5 \text{ }^{\circ}\text{C}^2 \text{ octave}^{-1}$, with shading incremented every half-contour. The curved dashed line (cone of influence) represents twice the e-folding time for the wavelet response to a spike in the timeseries; below this line the spectral density is underestimated due to edge effects. (c) Time-averaged spectra for the first half of the timeseries (green dashed) and the second half (black). (d) Running variance in the 0–1.4 year spectral band (green dashed) and the 1.4–8 year band (black). The total timeseries variance and total reconstructed wavelet variance are shown to the right of this panel.

tra are shown in Figs. 21 and 22. Both models exhibit strong interdecadal variations in the amplitude and period of ENSO, and interannual variations in the amplitude of the annual cycle. Many of the simulated ENSO events appear to be episodic, spanning a range of frequencies over the course of one or two events, rather than sustained oscillations. Both this episodic character and the interdecadal modulation of the dominant ENSO period contribute to the broad interannual peak in the time-mean spectrum.

It is clear from these figures that long timeseries are required to adequately characterize the ENSO spectrum in the models. In Figs. 21c and 22c, two time-averaged spectra are plotted—one for each half of the timeseries. Assuming that the NINO3 SST in these control runs is statistically stationary and that the two halves of the timeseries are nearly independent, then these two curves com-

prise a 50% confidence interval⁴ for timeseries of this length (150 years). At interannual periods this interval is still quite wide, even for 150-year timeseries. Thus subtle changes in the models' ENSO spectra, as might arise in climate change simulations, may be difficult to distinguish unless many ensemble members are used.

Even with timeseries of this length, however, it is easy to distinguish between the ENSO spectra of the models and observations, and between the two models. The simulated ENSOs are clearly too active, and compared to CM2.0, CM2.1 shows an even stronger ENSO which is shifted towards longer periods and is more strongly modulated from decade to decade.

⁴Select two values x_1, x_2 at random from a distribution with median θ . Then $P\{x_1 < \theta < x_2\} = 0.5 \times 0.5 = 0.25$, and similarly, $P\{x_2 < \theta < x_1\} = 0.25$. Thus the probability that x_1 and x_2 bracket θ is $0.25 + 0.25 = 0.5$.

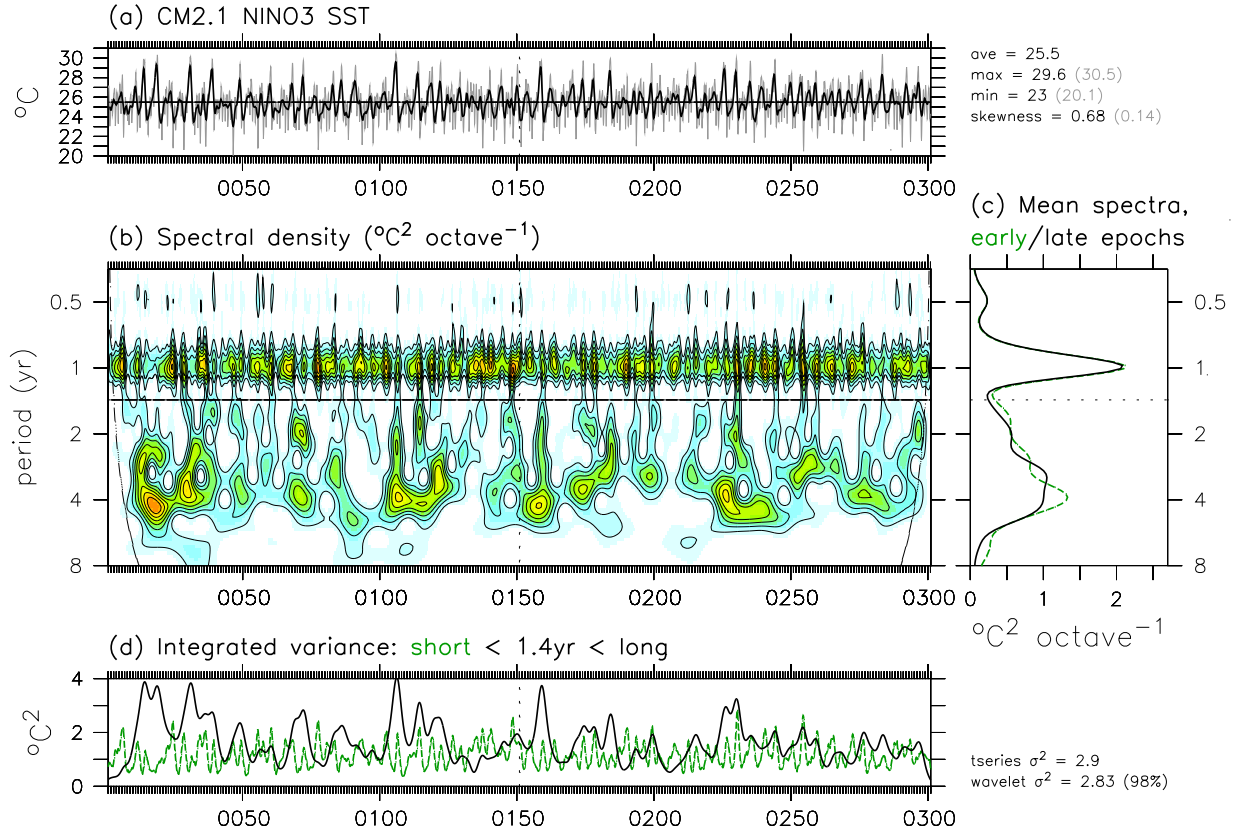


FIGURE 22: As in Fig. 21, but for CM2.1.

One possible cause for the excessive ENSO amplitude is the lack of a sufficient surface heat flux damping of SSTAs in the models (Figs. 18 and 19). Indeed, this damping is even weaker in CM2.1 than in CM2.0. Studies in a hierarchy of models (Zebiak and Cane 1987; Battisti and Hirst 1989; Wang and Weisberg 1996; Jin 1997a,b; Wittenberg 2002) have shown that reducing this heat flux damping tends to destabilize and amplify ENSO.

The differences in ENSO between CM2.0 and CM2.1 can also be connected to the differences in wind stress coupling (Fig. 17). Studies with intermediate models (An 2000; An and Wang 2000; Wang and An 2002; Wittenberg 2002) and a hybrid CGCM (Harrison et al. 2002) have demonstrated that shifting the τ'_x response eastward tends to increase the amplitude and period of ENSO, by enhancing positive air-sea feedbacks in the eastern Pacific and delaying the negative feedbacks associated with the slow adjustment of the equatorial thermocline. Other work (Kirtman 1997; An and Wang 2000; Wittenberg 2002) has described the sensitivity of ENSO to the meridional shape of the τ'_x response. A meridionally-wider τ'_x

response generates less wind stress curl close to the equator, weakening the delayed negative feedback associated with the slow adjustment of the zonal-mean thermocline depth, thereby producing a stronger ENSO with a longer period. Increasing the zonally-integrated strength of the wind stress feedback also tends to strengthen ENSO in realistic regimes (Zebiak and Cane 1987; Neelin 1991; Wakata and Sarachik 1994; Neelin et al. 1998). Thus the three differences between the CM2.0 and CM2.1 wind stress responses—the eastward shift, the meridional widening, and the strengthening of the τ'_x response in CM2.1—all appear to be consistent with the increased ENSO amplitude and period in CM2.1.

c. Skewness

The skewness statistics for the annual-mean and monthly-mean NINO3 SSTs are shown in Figs. 21 and 22, to the right of panel (a). As in observations, both models show a pronounced positive skewness of the inter-annual SSTs, with long, mild cold periods punctuated by

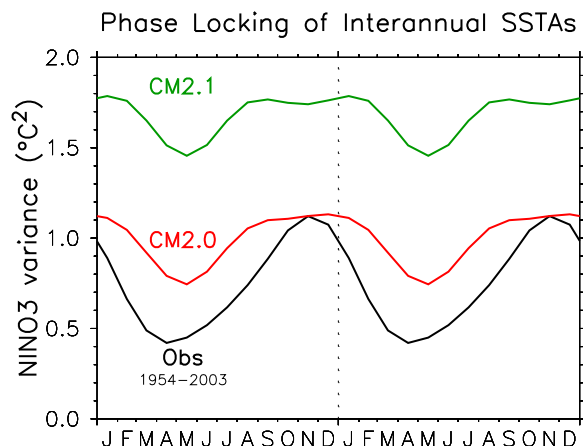


FIGURE 23: Seasonality of the interannual variance of NINO3-averaged SST anomalies, from observations, CM2.0, and CM2.1. The SSTs are filtered as in Fig. 15 prior to computing the variance. The horizontal axis spans two calendar cycles from January through December. Observations correspond to ER.v2 (Smith and Reynolds 2003).

short, extreme warm episodes⁵. Most other CGCMs substantially underestimate this skewness (Hannachi et al. 2003). The enhanced skewness in CM2.1 compared to CM2.0 is probably tied to the eastward shift of the precipitation and τ'_x responses (Figs. 16 and 17), which brings nonlinear coupled feedbacks into play in the eastern Pacific. Warm events shift west-Pacific convection eastward, generating stress anomalies where they can most effectively couple with the shallow oceanic thermocline via local upwelling; cold events, on the other hand, shift convection westward, generating only weak air-sea feedbacks in the eastern Pacific.

d. Seasonal phase locking

Fig. 23 shows the variance of interannual NINO3 SST anomalies as a function of calendar month. The observed NINO3 SSTs tend to peak near the end of the calendar year, with a variance maximum in November and a minimum in boreal spring. While the models do show a spring variance minimum, and a broad peak from August through February, the seasonal phase locking is not as strong and sharp as in the observations. The absence of a strong phase locking in the models is likely due to the relative lack of convective nonlinearity in the eastern Pacific, due to the equatorial cold bias and the westward shift of the mean and anomalous convection (Figs. 2, 4 and 16).

⁵The skewness of the annual-mean (monthly-mean) observed NINO3 SSTs is 0.47 (0.05) for ER.v2 1880–2004, and 0.85 (0.26) for OI.v2 1982–2004.

e. Evolution and mechanism

Fig. 24 shows a linear composite of ENSO, based on a set of NINO3 SSTA lag regressions for the models and for the GFDL/ARCs ocean analysis⁶. The observations show a nearly stationary growth of equatorial SSTs from the coast of South America to 160°E (Fig. 24a). The observed SSTs develop slightly earlier in the west than in the east (both about 12 months prior to the event peak) and then decay eastward about 9–12 months after the peak. At the event peak there are cold anomalies in the far western Pacific. There are also cold SSTs in the central Pacific both before and after the warm event.

The models exhibit a westward shift of the SSTA patterns relative to the observations. In the western and central Pacific, both models show the observed slightly westward-propagating cooling signature following the demise of the warm event (12 month lag), but show a subsequent cooling which is too strong and is shifted west of the observations. East of 120°W, CM2.0 shows less eastward propagation than observed, while CM2.1 captures this feature somewhat better.

In Fig. 24b, the observed equatorial zonal wind stress anomalies show a pronounced eastward-moving signature in the west/central Pacific, with precursor westerlies in the west evident up to 12 months prior to the NINO3 SSTA peak. The observed peak westerly anomalies occur near the dateline, about one month prior to the NINO3 SSTA peak, and at about the same time easterly anomalies begin developing in the far west. While CM2.0 and CM2.1 both show an eastward-moving signature in τ'_x , strong westerly anomalies do not propagate as far out into the Pacific basin as in the observations. (CM2.1 does show some improvement over CM2.0 in this regard.) Although the peak τ'_x is weak in the models, the zonal extent of the westerly anomalies is slightly broader than observed—since at the event peak the models have westerly anomalies in the far west Pacific instead of weak easterly anomalies as observed. CM2.1 gives a stronger τ'_x response than CM2.0, with both stronger westerlies in the western/central Pacific and stronger easterlies in the far eastern Pacific at the event peak.

As shown in Fig. 24c, the near-surface equatorial zonal currents in the observational assimilation are out of phase with NINO3 SST, with eastward currents peaking in the east Pacific about 5 months before the warm peak, and westward currents developing in the central and eastern Pacific at the warm peak and for the subsequent several months. Weak eastward currents are evident in the far west throughout the warm phase. The amplitude and phase of the zonal current anomalies are important, be-

⁶Although this linear composite refers to cold events as well, for simplicity we shall describe the evolution in terms of a warm event.

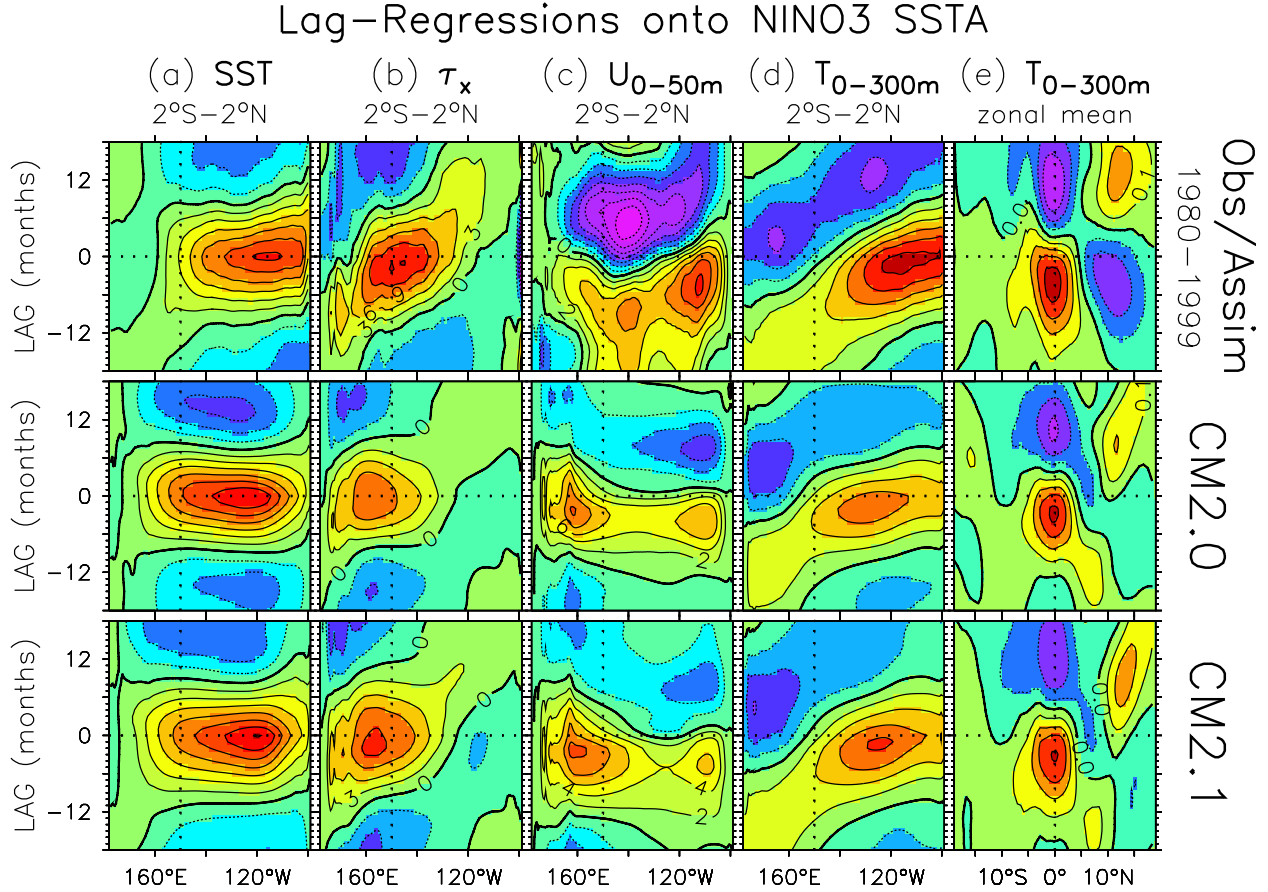


FIGURE 24: Lag regressions (per °C) onto NINO3-averaged SST anomalies. Time flows upward and spans a period of 36 months. Lag-0 (horizontal dotted line) indicates the NINO3 SSTA peak; positive lags correspond to the variable lagging NINO3 SSTAs in time, negative lags to the variable leading NINO3 SSTAs in time. Columns correspond to regressions for (a) SST (by 0.2°C) averaged 2°S–2°N, (b) zonal wind stress (by 3 mPa) averaged 2°S–2°N, (c) zonal currents (by 2 cm s⁻¹) averaged 2°S–2°N over the top 50 m of the ocean, (d) temperature (by 0.2°C) averaged 2°S–2°N over the top 300 m of the ocean, and (e) zonal-mean temperature (by 0.1°C) averaged zonally across the Pacific over the top 300 m of the ocean. First row corresponds to years 1980–1999 from ER.v2 for SST, from ERA40 for τ'_x , and from the GFDL/ARCs ocean analysis for the currents and subsurface temperatures. Second and third rows correspond to the CM2.0 and CM2.1 simulations.

cause they help transition the Pacific between warm and cold events by advecting on the strong background zonal SST gradient (Picaut et al. 1997; Jin and An 1999). Prior to the warming, eastward advection of the warm pool helps to warm the east; and after the event, westward advection of the cold tongue helps to restore the Pacific back toward equilibrium, often with an overshoot into a cold event. The models reproduce these features qualitatively, although the details are different. Both CM2.0 and CM2.1 show eastward current anomalies all along the equator up to 10 months prior to the warm peak (although these eastward current anomalies are somewhat weaker, and shifted farther westward, than in the analysis). The models also capture the observed reversal of these anomalies during the ENSO event. The westward anomalies in the central basin following the event

peak are also too weak, and are shifted farther east than in the analysis. That CM2.0 has stronger zonal current anomalies than CM2.1 in the central and eastern Pacific is likely tied to the narrower meridional structure of its τ'_x response (Fig. 17; Wittenberg 2002), and may partly explain its shorter period compared to CM2.1 (see Section 5b.).

In the assimilation, there is a slow eastward propagation of equatorial heat content anomalies (Fig. 24d), with a reduction of the zonal slope of the thermocline at the peak of El Niño. The models show similar features, although with weaker amplitude. This weaker thermocline variability is directly tied to the weak and westward-shifted τ'_x in the models (Fig. 17).

Fig. 24e shows a discharge of zonal-average heat content from the equator during El Niño, which occurs in the

models as well as in the observational analysis. The equatorial heat content peaks 3–4 months prior to the peak NINO3 SSTAs, at the same time that there is a deficit of heat content along 5° – 10° N. As the warm event peaks and then begins to decay, zonal-mean heat content is discharged from the equator to the north, so that 12 months after the event there is a deficit of heat content on the equator and positive heat content anomalies along 7° N– 15° N. Like the equatorial zonal current anomalies, the recharge/discharge of equatorial heat content is an important transitioner for ENSO (Jin 1997a). That the meridional recharge/discharge is stronger in CM2.0 than in CM2.1 may partly contribute to the shorter period in that model compared to CM2.1.

The lag regressions were also computed for the NCEP ocean analysis of Behringer et al. (1998). The evolution of subsurface anomalies in that analysis is similar to GFDL/ARCs (Fig. 24, first row), although the temperature and current anomalies in the east are weaker, and those in the west are stronger. The NCEP analysis also shows much weaker eastward zonal current anomalies in the central equatorial Pacific prior to the event peak.

6 ENSO teleconnections

a. Extratropical 200 hPa height field

The anomalous circulation associated with ENSO during the December-January-February (DJF) season is illustrated by the patterns of regression coefficients of 200 hPa height versus standardized NINO3 SSTAs (Fig. 25). These regression charts display the typical pattern and amplitude of 200 hPa height variations corresponding to a one-standard deviation change in the NINO3 index.

The observed distribution in Fig. 25a shows a familiar wavetrain, with two high centers located over the subtropical eastern Pacific and over Canada, and two low centers over in the eastern extratropical North Pacific and the southern U.S. This teleconnection pattern has been documented in detail by Horel and Wallace (1981) and others. The simulated amplitudes of the North Pacific and Canadian anomalies are weaker than the observed estimates by 20–30%. There is also a westward displacement (by 20 – 30° of longitude) of the North Pacific, Canadian, and southern U.S. centers in both CM2 simulations relative to the observed sites. In CM2.1, the low over the southern U.S. is no longer a distinct center, having merged with the low over the eastern extratropical North Pacific.

The westward shift of the simulated 200 hPa height anomalies is likely tied to the excessive westward spread of the SST anomalies and associated precipitation changes during the simulated ENSO events (Section 5,

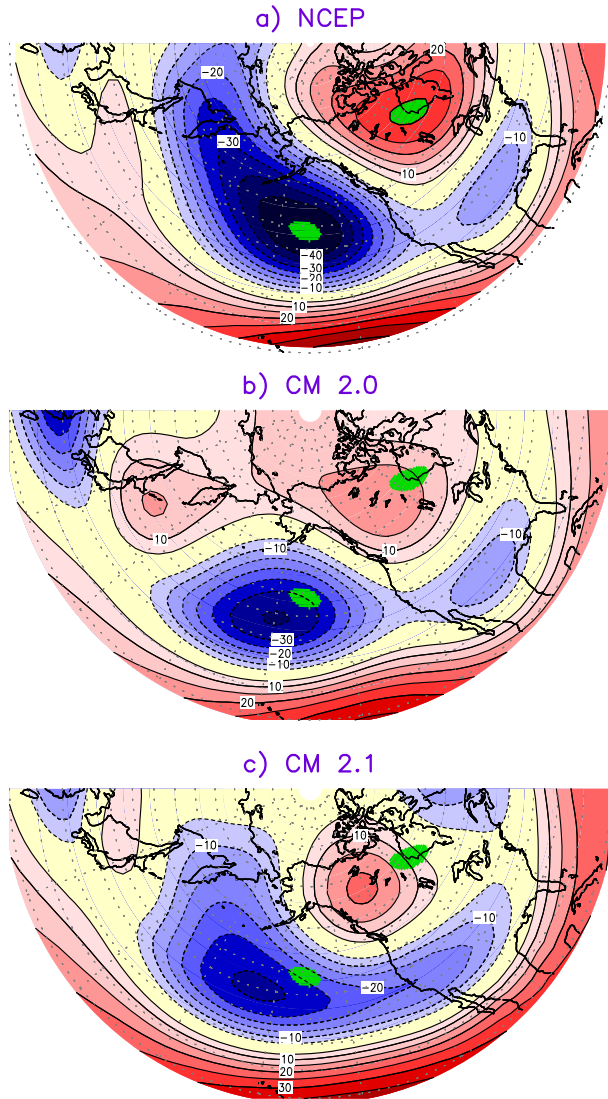


FIGURE 25: Regressions of 200 hPa heights onto standardized NINO3 SSTAs for the December-January-February season, computed using (a) the NCEP/NCAR Reanalysis (Kistler et al. 2001) for 1951–2000, (b) CM2.0, and (c) CM2.1. Contour interval is 5 m, and the zero contour is not plotted. Green shading in all panels indicates the positions of the NCEP extrema over the North Pacific and Canada.

Figs. 15 and 16, and Fig. 26). The corresponding patterns generated by subjecting the atmospheric component of CM2.0 to observed SST forcing exhibit noticeably less model bias in the positions of the anomaly centers (Fig. 14 of GAMDT 2005). It is also noteworthy that in the atmosphere-only simulation, the extratropical wave-train for the 1957–58 event (where the peak SSTA was located near 150° W– 180° W) was displaced well to the west of the corresponding feature for the 1997–98 event (where the peak SSTA occurred near the South American coast, 90° W– 120° W). In both observed and simu-

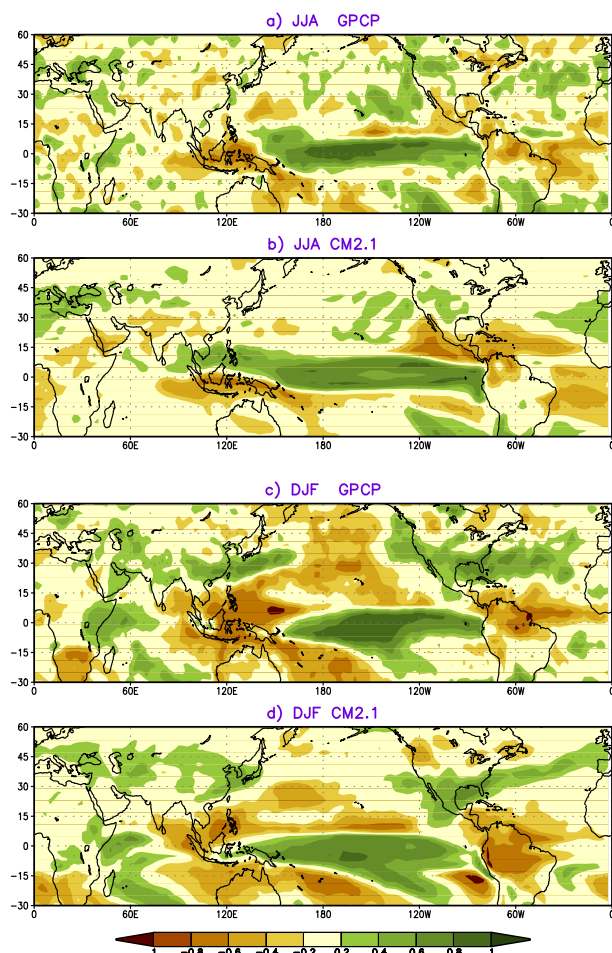


FIGURE 26: Correlations of precipitation with NINO3 SSTs for (a,b) June-July-August and (c,d) December-January-February, computed using (a,c) observational estimates from GPCP.v1 (Huffman et al. 1997) for 1979–2000, and (b,d) output from CM2.1. Green (brown) shading highlights wet (dry) anomalies with absolute correlation values exceeding 0.2, which corresponds to a significance level of 95% for the model data.

lated atmospheres, such longitudinal shifts in the wave trains strongly affect the inter-event variability of the patterns of temperature and precipitation changes over North America (Hoerling and Kumar 2002).

b. Precipitation field

Seasonal correlations between precipitation and NINO3 SSTs are displayed in Fig. 26. The CM2.0 results (not shown) are similar to those for CM2.1. Use of the correlation (as opposed to regression) coefficients is intended to more clearly reveal the precipitation features in the subtropics and midlatitudes, where the precipitation anomalies are weaker than those in the deep tropics.

As noted in GAMDT (2005) and Section 5, the simulated positive precipitation anomaly in the equatorial Pacific extends too far west to the Indonesian Archipelago during warm events in both seasons (Figs. 26b and 26d); whereas the corresponding observations (Figs. 26a and 26c) indicate much drier conditions over Indonesia, as well as over the South China and Philippine Seas.

During the June-July-August season, both model and observations (Figs. 26a and 26b) show dry anomalies over Central America and the surrounding waters, as well as the equatorial Atlantic and the northern part of South America. There is also some weaker indication of suppressed rainfall over parts of the South Asian monsoon regions during warm ENSO events.

Figs. 26c and 26d show that in DJF, the model agrees well with observations regarding the northeastward shift of the SPCZ rainfall during warm ENSO events. The dry conditions over the Bay of Bengal, South China Sea, western Indonesia, northern Australia, equatorial South America, and southern Africa are also captured by the model, as are the above-normal precipitation over southeastern China and the East China Sea, eastern equatorial Africa, and a broad belt extending eastward from the U.S. western seaboard across northern Mexico to the Gulf Coast and subtropical Atlantic. The precipitation features over East Asia are related to the anomalous near-surface anticyclone centered near the Philippine Sea during warm ENSO events (Wang et al. 2000). The enhanced precipitation over the southern part of North America and the surrounding maritime areas is associated with the higher frequency of synoptic-scale disturbances traveling along the deepened stationary trough over that region (Fig. 25).

7 Conclusions

We have described multicentury control runs from the GFDL global coupled ocean/atmosphere/land/ice models, CM2.0 and CM2.1, in terms of their tropical Pacific climate, seasonal cycle, ENSO variability, and ENSO teleconnections. We conclude that substantial progress has been made toward realistic simulation of these features, though some challenges remain.

1. Most of the key features of the observed climate and variability of tropical Pacific SST, trade winds and precipitation, surface heat fluxes, surface currents, equatorial undercurrent, and subsurface thermal structure are well captured by the models.
2. Annual-mean SST biases in the control simulations include a warm bias along the coast of South America, a modest cold bias along the equator, and a slight warm bias in the vicinity of the ITCZ.

3. The simulated annual-mean surface fluxes of water, heat, and momentum are in reasonable agreement with observations. Problems include a dry bias at the equator with too much insolation over the central and eastern Pacific; excessive precipitation south of the equator in the east Pacific; a westward shift of the trade winds resulting in too much evaporation west of the dateline; and weaker-than-observed southerly winds with too little evaporation near the coast of South America.
4. The simulated equatorial annual-mean subsurface temperatures are quite realistic at the equator, with the thermocline at approximately the right depth. However, the thermocline is too diffuse in the vertical and shows a slightly stronger zonal slope than in observations, with strong near-surface stratification along the coast of South America. The simulated zonal-mean annual-mean thermocline is meridionally too flat.
5. The annual-mean EUC is well simulated. The mean surface current patterns are shifted 20–30° west of those observed, and the SEC and NECC are too weak in the eastern Pacific.
6. The simulations show a robust, westward-propagating annual cycle of SST and zonal winds along the equator, which is in good qualitative agreement with observations. An overly strong semiannual component of the zonal winds, however, generates a similar semiannual signal in the equatorial zonal currents. In the eastern Pacific, the off-equatorial annual cycle is too strong—in boreal spring, excessive SSTs and rainfall south of the equator contribute to an unrealistic reversal of the equatorial meridional winds.
7. The models have a robust ENSO with multidecadal fluctuations in amplitude, an irregular period between 2 and 5 years, and SST anomalies that are skewed toward warm events as observed. The evolution of ENSO subsurface temperatures is quite realistic, as are the ENSO correlations with precipitation anomalies outside the tropical Pacific. However, the simulated ENSOs are too strong, too weakly damped by surface heat fluxes, and are not sufficiently phase-locked to the end of the calendar year. The simulated ENSO patterns of SST, wind stress, and precipitation variability are shifted 20°–30° west of the observed patterns. Such problems appear to be linked to the model mean state biases—namely the equatorial cold bias, the double ITCZ, and the over-stratified surface waters near the South American coast.
8. Relative to observations, the models show a 20°–30° westward shift of the ENSO teleconnections to northern hemisphere 200 hPa heights during winter, related to the westward shift of the ENSO tropical rainfall anomalies.
9. By several measures, CM2.0 outperforms CM2.1 in the tropical Pacific, with reduced SST biases near the equator and the South American coast, more realistic surface insolation at the equator, reduced off-equatorial subsurface temperature biases, a less intense double ITCZ, stronger annual-mean surface currents, a more realistic annual cycle, and a less intense ENSO. CM2.1, on the other hand, shows a reduced warm bias below the equatorial thermocline, reduced precipitation biases in the SPCZ and northern ITCZ, a longer-period ENSO with less westward displacement of the variability relative to observations, and a strong skewness of ENSO SST anomalies toward warm events as observed.

Acknowledgments. Tom Knutson, Gabriel Vecchi, Ron Stouffer, Steve Klein, and Tony Gordon provided insightful comments that greatly improved this paper. The authors thank the providers of the observational datasets: ECMWF for the ERA40 reanalysis; NCEP, CPC, and the IRI Climate Data Library for the NOAA OI.v2 SSTs, CMAP precipitation, UWM/COADS heat fluxes, and NCEP Pacific Ocean subsurface analysis; NOAA-CIRES CDC for the NCEP/NCAR Reanalysis, NCEP/DOE Reanalysis, and ER.v2 SSTs; NASA/GSFC and NCDC for the GPCP precipitation; IFREMER/CERSAT for the SeaWinds/QuikSCAT winds; FSU/COAPS for the FSU pseudostresses; the Southampton Oceanography Centre for the SOC heat fluxes; K. Trenberth and D. Stepaniak for the ERBE/NCEP heat flux; SMST/Tokai Univ. for the J-OFURO heat fluxes; MPI for the HOAPS-II heat fluxes; the ESR OSCAR Project Office for surface current data; and the PMEL TAO Project Office for subsurface current data. We also thank the members of GFDL Modeling Services for their assistance with model infrastructure support and data processing. Wavelet analyses were produced using Fortran codes provided by C. Torrence and G. Compo at paos.colorado.edu/research/wavelets.

REFERENCES

- AchutaRao, K., and K. R. Sperber, 2002: Simulation of the El Niño Southern Oscillation: Results from the Coupled Model Intercomparison Project. *Climate Dyn.*, **19**, 191–209.
- AchutaRao, K., K. R. Sperber, and the CMIP modeling groups, 2000: El Niño Southern Oscillation in coupled GCMs. PCMDI Report 61, PCMDI, LLNL, University of California, Livermore, CA 94550, USA.

- Alexander, M. A., I. Blade, M. Newman, J. R. Lanzante, N.-C. Lau, and J. D. Scott, 2002: The atmospheric bridge: The influence of ENSO teleconnections on air-sea interaction over the global oceans. *J. Climate*, **15**, 2205–2231.
- An, S.-I., 2000: On the slow mode of a simple air-sea coupled model: the sensitivity to the zonal phase difference between the SST and the atmospheric heating. *J. Meteor. Soc. Japan*, **78**, 159–165.
- An, S.-I., and B. Wang, 2000: Interdecadal change of the structure of the ENSO mode and its impact on the ENSO frequency. *J. Climate*, **13**, 2044–2055.
- Atlas, R., R. N. Hoffman, S. C. Bloom, J. C. Jusem, and J. Ardizzone, 1996: A multiyear global surface wind velocity dataset using SSM/I wind observations. *Bull. Amer. Meteor. Soc.*, **77**, 869–882.
- Barnett, T. P., M. Latif, E. Kirk, and E. Roeckner, 1991: On ENSO physics. *J. Climate*, **4**, 487–515.
- Barsugli, J. J., and P. D. Sardeshmukh, 2002: Global atmospheric sensitivity to tropical SST anomalies throughout the Indo-Pacific basin. *J. Climate*, **15**, 3427–3442.
- Battisti, D. S., and A. C. Hirst, 1989: Interannual variability in a tropical atmosphere-ocean model: Influence of the basic state, ocean geometry and nonlinearity. *J. Atmos. Sci.*, **46**, 1687–1712.
- Behringer, D. W., M. Ji, and A. Leetmaa, 1998: An improved coupled model for ENSO prediction and implications for ocean initialization. Part I: The ocean data assimilation system. *Mon. Wea. Rev.*, **126**, 1013–1021.
- Bonjean, F., and G. S. E. Lagerloef, 2002: Diagnostic model and analysis of the surface currents in the tropical Pacific ocean. *J. Phys. Oceanogr.*, **32**, 2938–2954.
- Bourassa, M. A., S. R. Smith, and J. J. O'Brien, 2001: A new FSU winds and flux climatology. *11th Conference on Interactions of the Sea and Atmosphere*, San Diego, CA, 9–12. Amer. Meteor. Soc.
- Cole, J., 2001: A slow dance for El Niño. *Science*, **291**, 1496–1497.
- da Silva, A. M., C. C. Young, and S. Levitus, 1994: Atlas of Surface Marine Data 1994, Vol. 1: Algorithms and Procedures. NOAA Atlas NESDIS 6, U.S. Department of Commerce, Washington, D.C.
- Davey, M. K., M. Huddleston, K. R. Sperber, and model data contributors, 2000: STOIC: A study of coupled GCM climatology and variability in tropical ocean regions. STOIC project report, CLIVAR-WGSIP.
- Davey, M. K., M. Huddleston, K. R. Sperber, and model data contributors, 2002: STOIC: A study of coupled model climatology and variability in tropical ocean regions. *Climate Dyn.*, **18**, 403–420.
- Delworth, T. L., A. J. Broccoli, A. Rosati, R. J. S. V. Balaji, J. A. Beesley, W. F. Cooke, K. W. Dixon, J. Dunne, K. A. Dunne, J. W. Durack, K. L. Findell, P. Ginoux, A. Gnanadesikan, C. T. Gordon, S. M. Griffies, R. Gudgel, M. J. Harrison, I. M. Held, R. S. Hemler, L. W. Horowitz, S. A. Klein, T. R. Knutson, P. J. Kushner, A. L. Langenhorst, H.-C. Lee, S. J. Lin, J. Lu, S. L. Malyshev, P. C. Milly, V. Ramaswami, J. Russell, M. D. Schwarzkopf, E. Shevliakova, J. Sirutis, M. Spelman, W. F. Stern, M. Winton, A. T. Wittenberg, B. Wyman, F. Zeng, and R. Zhang, 2005: GFDL's CM2 global coupled climate models, Part 1: Formulation and simulation characteristics. Submitted to *J. Climate*.
- Derber, J., and A. Rosati, 1989: A global oceanic data assimilation system. *J. Phys. Oceanogr.*, **19**, 1333–1347.
- Diaz, H. F., and V. Markgraf, eds., 2000: *El Niño and the Southern Oscillation: Multiscale variability and its impacts on natural ecosystems and society*. Cambridge University Press, Cambridge U.K. 496pp.
- Dijkstra, H. A., and J. D. Neelin, 1995: Ocean-atmosphere interaction and the tropical climatology. Part II: Why the Pacific cold tongue is in the east. *J. Climate*, **8**, 1343–1359.
- Easterling, D. R., G. A. Meehl, C. Parmesan, S. A. Changnon, T. R. Karl, and L. O. Mearns, 2000: Climate extremes: Observations, modeling, and impacts. *Science*, **289**, 2068–2074.
- Fedorov, A. V., and S. G. Philander, 2000: Is El Niño changing? *Science*, **288**, 1997–2002.
- GAMDT (GFDL Global Atmospheric Model Development Team), 2005: The new GFDL global atmosphere and land model AM2/LM2: Evaluation with prescribed SST simulations. *J. Climate*, **18**, in press.
- Gent, P. R., and J. C. McWilliams, 1990: Isopycnal mixing in ocean circulation models. *J. Phys. Oceanogr.*, **20**, 150–155.
- Gnanadesikan, A., K. W. Dixon, S. M. Griffies, V. Balaji, J. A. Beesley, W. F. Cooke, T. L. Delworth, M. J. Harrison, I. M. Held, W. J. Hurlin, H.-C. Lee, Z. Liang, G. Nong, R. C. Pacanowski, A. Rosati, J. Russell, B. L. Samuels, S. M. Song, M. J. Spelman, R. J. Stouffer, C. O. Sweeney, G. Vecchi, M. Winton, A. T. Wittenberg, R. Zhang, and F. Zheng, 2005: GFDL's CM2 global coupled climate models, Part 2: The baseline ocean simulation. Submitted to *J. Climate*.
- Goddard, L., S. J. Mason, S. E. Zebiak, C. F. Ropelewski, R. Basher, and M. A. Cane, 2001: Current approaches to seasonal to interannual climate predictions. *Int. J. Climatol.*, **21**, 1111–1152.
- Grassl, H., V. Jost, R. Kumar, J. Schulz, P. Bauer, and P. Schluessel, 2000: The Hamburg Ocean-Atmosphere Parameters and Fluxes from Satellite Data (HOAPS): A Climatological Atlas of Satellite-Derived Air-Sea-Interaction Parameters over the Oceans. Technical Report 312, Max Planck Institute for Meteorology, Hamburg, Germany. ISSN 0937-1060.
- Griffies, S. M., 1998: The Gent-McWilliams skew flux. *J. Phys. Oceanogr.*, **28**, 831–841.
- Griffies, S. M., A. Gnanadesikan, R. C. Pacanowski, V. D. Larichev, J. K. Dukowicz, and R. D. Smith, 1998: Isoneutral diffusion in a z-coordinate ocean model. *J. Phys. Oceanogr.*, **28**, 805–830.
- Griffies et al., 2005: Formulation of an ocean model for global climate simulations. To be submitted to *Ocean Modelling*.
- Grist, J. P., and S. A. Josey, 2003: Inverse analysis adjustment of the SOC air-sea flux climatology using ocean heat transport constraints. *J. Climate*, **16**, 3274–3295.
- Hannachi, A., D. B. Stephenson, and K. R. Sperber, 2003: Probability-based methods for quantifying nonlinearity in the ENSO. *Climate Dyn.*, **20**, 241–256.
- Harrison, M. J., A. Rosati, B. J. Soden, E. Galanti, and E. Tziperman, 2002: An evaluation of air-sea flux products for ENSO simulation and prediction. *Mon. Wea. Rev.*, **130**, 723–732.
- Hoerling, M. P., and A. Kumar, 2002: Atmospheric response patterns associated with tropical forcing. *J. Climate*, **15**, 2184–2203.
- Horel, J. D., and J. M. Wallace, 1981: Planetary-scale atmospheric phenomena associated with the Southern Oscillation. *Mon. Wea. Rev.*, **109**, 813–829.
- Hsu, H.-H., and A. D. Moura, 2001: Workshop on the impacts of the 1997–99 ENSO. *Bull. Amer. Meteor. Soc.*, **82**, 305–312.
- Huffman, G. J., R. F. Adler, P. Arkin, A. Chang, R. Ferraro, A. Gruber, J. Janowiak, A. McNab, B. Rudolf, and U. Schneider, 1997: The Global Precipitation Climatology Project (GPCP) combined precipitation dataset. *Bull. Amer. Meteor. Soc.*, **78**, 5–20.
- IFREMER/CERSAT, 2002: QuikSCAT Scatterometer Mean Wind Field Products User Manual. C2-MUT-W-04-IF, version 1.0, IFREMER/CERSAT, Plouzane, France.
- IPCC, 2001: *Climate Change 2001: The Scientific Basis. Contribution of Working Group I to the Third Assessment Report of the Intergovernmental Panel on Climate Change* [Houghton, J. T., Y. Ding, D. J. Griggs, M. Noguer, P. J. van der Linden, X. Dai, K. Maskell, and C. A. Johnson (eds.)]. Cambridge University Press, Cambridge, United Kingdom and New York, NY, USA. 881pp.
- Jin, F.-F., 1997a: An equatorial ocean recharge paradigm for ENSO. Part I: Conceptual model. *J. Atmos. Sci.*, **54**, 811–829.
- Jin, F.-F., 1997b: An equatorial ocean recharge paradigm for ENSO. Part II: A stripped-down coupled model. *J. Atmos. Sci.*, **54**, 830–847.
- Jin, F.-F., and S.-I. An, 1999: Thermocline and zonal advective feedbacks within the equatorial ocean recharge oscillator model for ENSO. *Geophys. Res. Lett.*, **26**, 2989–2992.

- Josey, S. A., E. C. Kent, and P. K. Taylor, 1998: The Southampton Oceanography Centre (SOC) Ocean - Atmosphere Heat, Momentum and Freshwater Flux Atlas. Technical Report 6, Southampton Oceanography Centre.
- Kirtman, B. P., 1997: Oceanic Rossby wave dynamics and the ENSO period in a coupled model. *J. Climate*, **10**, 1690–1704.
- Kistler, R., W. Collins, S. Saha, G. White, J. Woollen, E. Kalnay, M. Chelliah, W. Ebisuzaki, M. Kanamitsu, V. Kousky, H. van den Dool, R. Jenne, and M. Fiorino, 2001: The NCEP-NCAR 50-year reanalysis: Monthly means CD-ROM and documentation. *Bull. Amer. Meteor. Soc.*, **82**, 247–268.
- Kubota, M., N. Iwasaka, S. Kizu, M. Konda, and K. Kutsuwada, 2002: Japanese ocean flux data sets with use of remote sensing observations (J-OFURO). *J. Oceanogr.*, **58**, 213–225.
- Large, W. G., G. Danabasoglu, J. C. McWilliams, P. R. Gent, and F. O. Bryan, 2001: Equatorial circulation of a global ocean climate model with anisotropic horizontal viscosity. *J. Phys. Oceanogr.*, **31**, 518–536.
- Large, W. G., J. C. McWilliams, and S. C. Doney, 1994: Oceanic vertical mixing: A review and a model with a vertical K-profile boundary layer parameterization. *Rev. Geophys.*, **32**, 363–403.
- Latif, M., D. Anderson, T. Barnett, M. Cane, R. Kleeman, A. Leetmaa, J. O'Brien, A. Rosati, and E. Schneider, 1998: A review of the predictability and prediction of ENSO. *J. Geophys. Res.*, **103**, 14 375–14 393.
- Latif, M., K. Sperber, and CMIP participants, 2001: ENSIP: The El Niño Simulation Intercomparison Project. *Climate Dyn.*, **18**, 255–276.
- Lin, S.-J., 2004: A “vertically Lagrangian” finite-volume dynamical core for global models. *Mon. Wea. Rev.*, **132**, 2293–2307.
- Lock, A. P., A. R. Brown, M. R. Bush, G. M. Martin, and R. N. B. Smith, 2000: A new boundary layer mixing scheme. Part I: Scheme description and single-column model tests. *Mon. Wea. Rev.*, **128**, 3187–3199.
- McPhaden, M. J., A. J. Busalacchi, R. Cheney, J.-R. Donguy, K. S. Gage, D. Halpern, M. Ji, P. Julian, G. Meyers, G. T. Mitchum, P. P. Niiler, J. Picaut, R. W. Reynolds, N. Smith, and K. Takeuchi, 1998: The Tropical Ocean-Global Atmosphere observing system: A decade of progress. *J. Geophys. Res.*, **103**, 14 169–14 240.
- Moore, A. M., 1995: Tropical interannual variability in a global coupled GCM: sensitivity to mean climate state. *J. Climate*, **8**, 807–828.
- Moorthi, S., and M. J. Suarez, 1992: Relaxed Arakawa-Schubert: A parameterization of moist convection for general circulation models. *Mon. Wea. Rev.*, **120**, 978–1002.
- Morel, A., and D. Antoine, 1994: Heating rate within the upper ocean in relation to its bio-optical state. *J. Phys. Oceanogr.*, **24**, 1652–1665.
- Neelin, J. D., 1991: The slow sea surface temperature mode and the fast-wave limit: Analytic theory for tropical interannual oscillations and experiments in a hybrid coupled model. *J. Atmos. Sci.*, **48**, 584–606.
- Neelin, J. D., D. S. Battisti, A. C. Hirst, F.-F. Jin, Y. Wakata, T. Yamagata, and S. Zebiak, 1998: ENSO theory. *J. Geophys. Res.*, **103**, 14 261–14 290.
- Philander, S. G. H., D. Gu, D. Halpern, G. Lambert, N.-C. Lau, T. Li, and R. C. Pacanowski, 1996: Why the ITCZ is mostly north of the equator. *J. Climate*, **9**, 2958–2972.
- Picaut, J., F. Masia, and Y. du Penhoat, 1997: An advective-reflective conceptual model for the oscillatory nature of the ENSO. *Science*, **277**, 663–666.
- Reynolds, R. W., N. A. Rayner, T. M. Smith, D. C. Stokes, and W. Wang, 2002: An improved in situ and satellite SST analysis for climate. *J. Climate*, **15**, 1609–1625.
- Rothstein, L. M., D. L. T. Anderson, E. S. Sarachik, and P. J. Webster, 1998: The TOGA Decade: Reviewing the progress of El Niño research and prediction. *J. Geophys. Res.*, **103**, 14 167–14 510.
- Simmons, A. J., and J. K. Gibson, 2000: ERA-40 Project Report Series No. 1: The ERA-40 Project Plan. Technical Report, ECMWF, Shinfield Park, Reading, United Kingdom.
- Smith, S. R., J. Servain, D. M. Legler, J. N. Stricherz, M. A. Bourassa, and J. J. O'Brien, 2004: Quantifying uncertainties in NCEP reanalyses using high-quality research vessel observations. *Bull. Amer. Meteor. Soc.*, **85**, 979–994.
- Smith, T. M., and R. W. Reynolds, 2003: Extended reconstruction of global sea surface temperatures based on COADS data (1854–1997). *J. Climate*, **16**, 1495–1510.
- Stouffer, R. J., A. J. Broccoli, T. L. Delworth, K. W. Dixon, R. Gudgel, I. Held, R. Hemler, T. Knutson, H.-C. Lee, M. D. Schwarzkopf, B. Soden, M. J. Spelman, M. Winton, and F. Zeng, 2005: GFDL's CM2 global coupled climate models, Part 4: Climate response to a 1% increase in atmospheric CO₂ concentration. Submitted to *J. Climate*.
- Stricherz, J. N., D. M. Legler, and J. J. O'Brien, 1997: TOGA pseudostress atlas 1985–1994. II: Tropical Pacific Ocean. COAPS Tech. Rep. 97-2, COAPS/The Florida State University, Tallahassee, FL.
- Sun, D.-Z., T. Zhang, C. Covey, S. Klein, W. Collins, J. Hack, J. Kiehl, J. Meehl, I. Held, and M. Suarez, 2005: Radiative and dynamical feedbacks over the equatorial cold tongue: Results from seven atmospheric GCMs. Submitted to *J. Climate*.
- Sweeney, C., A. Gnanadesikan, S. M. Griffies, M. J. Harrison, A. J. Rosati, and B. L. Samuels, 2004: Impacts of shortwave penetration depth on large-scale ocean circulation and heat transport. *J. Phys. Oceanogr.* In press.
- Trenberth, K. E., J. M. Caron, and D. P. Stepaniak, 2001: The atmospheric energy budget and implications for surface fluxes and ocean heat transports. *Climate Dyn.*, **17**, 259–276.
- Tudhope, A. W., C. P. Chilcott, M. T. McCulloch, E. R. Cook, J. Chappell, R. M. Ellam, D. W. Lea, J. M. Lough, and G. B. Shimmield, 2001: Variability in the El Niño-Southern Oscillation through a glacial-interglacial cycle. *Science*, **291**, 1511–1517.
- Wakata, Y., and E. S. Sarachik, 1994: Nonlinear effects in coupled atmosphere-ocean basin modes. *J. Atmos. Sci.*, **51**, 909–920.
- Wang, B., and S.-I. An, 2002: A mechanism for decadal changes of ENSO behavior: Roles of background wind changes. *Climate Dyn.*, **18**, 475–486.
- Wang, B., R. Wu, and X. Fu, 2000: Pacific-East Asian teleconnection: How does ENSO affect East Asian climate? *J. Climate*, **13**, 1517–1211.
- Wang, C., and R. H. Weisberg, 1996: Stability of equatorial modes in a simplified coupled ocean-atmosphere model. *J. Climate*, **9**, 3132–3148.
- Wittenberg, A. T., 2002: *ENSO Response to Altered Climates*. Ph.D. thesis, Princeton University. 475pp.
- Wittenberg, A. T., 2004: Extended wind stress analyses for ENSO. *J. Climate*, **17**, 2526–2540.
- Xie, P., and P. A. Arkin, 1996: Analyses of global monthly precipitation using gauge observations, satellite estimates, and numerical model predictions. *J. Climate*, **9**, 840–858.
- Xie, P., and P. A. Arkin, 1997: Global precipitation: A 17-year monthly analysis based on gauge observations, satellite estimates, and numerical model outputs. *Bull. Amer. Meteor. Soc.*, **78**, 2539–2558.
- Zebiak, S. E., and M. A. Cane, 1987: A model El Niño-Southern Oscillation. *Mon. Wea. Rev.*, **115**, 2262–2278.